Laboratory volcano geodesy

by

Rikke Færøvik Johannessen

*Image: Saint Helena Volcano
(www.goodwp.com/nature/16303-volcano-dust-smoke-mountains-saint-helena-island.html)

Laboratory volcano geodesy

by

Rikke Færøvik Johannessen

THESIS

FOR THE DEGREE OF

MASTER OF SCIENCE

(Physics of geological Processes, Department of Geology)

Faculty of Mathematics and Natural Sciences
University of Oslo

June 2014

"Civilization exists by geological consent, subject to change without notice."

Will Durant

UNIVERSITY OF OSLO

Abstract

Faculty of Mathematics and Natural Sciences
Department of Geology

Master of Science

Laboratory volcano geodesy

by Rikke Færøvik Johannessen

Magma transport in volcanic plumbing systems induces surface deformation, which can be monitored by geodetic techniques, such as GPS and InSAR. These geodetic signals are commonly analyzed through geodetic models in order to constrain the shape of, and the pressure in, magma plumbing systems. These models, however, suffer critical limitations: (1) the modelled magma conduit shapes cannot be compared with the real conduits, so the geodetic models cannot be tested nor validated; (2) the modelled conduits only exhibit shapes that are too simplistic; (3) most geodetic models only account for elasticity of the host rock, whereas substantial plastic deformation is known to occur. To overcome these limitations, one needs to use a physical system, in which (1) both surface deformation and the shape of, and pressure in, the underlying conduit are known, and (2) the mechanical properties of the host material are controlled and well known.

In this contribution, we present novel quantitative laboratory results of shallow magma emplacement. Fine-grained silica flour represents the brittle crust, and low viscosity vegetable oil is an analogue for the magma. The melting temperature of the oil is 31 °C; the oil solidifies in the models after the end of the experiments. At the time of injection the oil temperature is 50 °C. The oil is pumped from a reservoir using a volumetric pump into the silica flour through a circular inlet at the bottom of a 40x40 cm square box. The silica flour is cohesive, such that oil intrudes it by fracturing it, and produces typical sheet intrusions (dykes, cone sheets, etc.). During oil intrusion, the model surface deforms, mostly by doming. These movements are measured by an advanced photogrammetry method, which uses 4 synchronized fixed cameras that periodically image the surface of the model from

different angles. We apply particle tracking method to compute the 3D ground deformation pattern through time. After solidification of the oil, the intrusion can be excavated and photographed from several angles to compute its 3D shape with the same photogrammetry method. Then, the surface deformation pattern can be directly compared with the shape of underlying intrusion. This quantitative dataset is essential to quantitatively test and validate classical volcano geodetic models.

Acknowledgements

I would like to thank Olivier Galland, my supervisor, for much needed help and guidence. I appreciate your honest opinion and enthusiasm.

To Fabian, my boyfriend who has supported me all the way, despite my long days at school and my distant mind when at home: I could never have done this without you! A big thanks to Kaia and Pernille for the friendship, mental support and for pushing me to have faith in myself. Thanks to my lovely family who supports me in all my impulsive and ever-changing decisions, for understanding my interest in geology and for beeing proud of me.

I would like to thank my classmate, Maria, for beeing my partner the first year, for sharing my frustration and passion for this field of geology, and everything that comes along. Thank you to my pack of international students who brought me in as one of them, and let me practise my english in my everso Norwegian life. Thanks to Anne and Sigve for enlightening conversations in fields I never knew existed, for bringing me out of this study cave during lunch hours and for showing interest and giving me feedback on my thesis.

Thanks to Hedda and Kerstin for recommending me to write my thesis in LaTex, it made the whole writing process everything much easier.

Contents

List of Figures

Chapter 1

Introduction

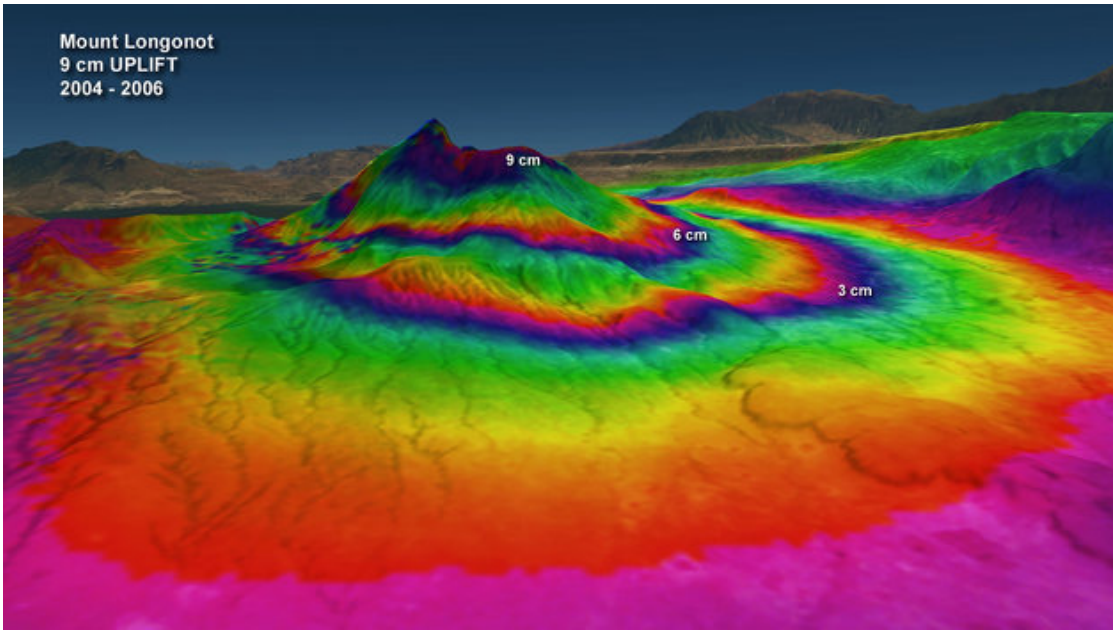

FIGURE 1.1: InSAR Image showing the deformation of the volcano Longonot by the East-African rift between 2004 and 2006 (Envisat AutoC2) (Duyck, 2014).

How can we predict the location of the next volcanic eruption by looking at the deformation pattern acquired by geodetic methods? How valid are geodetic inversion models used for modeling the magmatic plumbing system after a volcanic event? Which deformation patterns are related to the different complex shapes of magmatic intrusions? Monitoring the surface dynamics of volcanoes to constrain the shape and size of the magmatic conduit has been performed in more than half a century (Amelung et al., 2000; Cayol and Cornet, 1998; Lu et al., 2010; Mogi, 1958; Okada, 1985; Pedersen and Sigmundsson, 2006; Segall et al., 2001;

Sigmundsson et al., 1992, 2010). The most common geodetic methods are tilt meter, GPS, Photogrammetry and InSAR. These methods require simplifying assumptions, post-data processing and then modeling by using the best fit. We can't quantitatively test the geodetic models without physically entering the plumbing systems of the volcano! To overcome these limitations, we need to use a physical system, in which (1) both surface deformation and the shape of, and pressure in, the underlying conduit are known, and (2) the mechanical properties of the host material are controlled and well known.

Analogue models have been used for modeling surface deformation of volcanoes, using both gelatin models (Donnadieu et al., 2003; Kavanagh et al., 2006; Rivalta et al., 2005; Takada, 1990, 1994) and granular material (Abdelmalak et al., 2012; Galland, 2012; Galland et al., 2007, 2006, 2003; Gressier, 2010; Mathieu et al., 2008; Tortini et al., 2013) as crustal analogues.

Here we presents a new method for monitoring and analyzing surface deformation data, and applies it to an analogue model where materials used can be excavated to reveal the subsurface shapes. The method was tested on six experiments with the analogue model, using the same parameters. Chapter 2: Theoretical background, provides a short summary of the geodetic methods used for data acquisition, continuing with the data processing and modeling. Then we present what has been done within analogue modeling considering materials and method of monitoring surface deformation during the experiment. In chapter 3, Laboratory volcano geodesy, the experimental setup that was developed and published by Galland (2012); Galland et al. (2006, 2009) is presented and explained step by step, including the new photogrammetric setup first presented here in this thesis. Chapter 4, Photogrammetric analysis, presents and explains in detail the new analysis of the photogrammetric data including the use of the open-source photogrammetry tool of Micmac and the following matlab analysis using the outputs from the MicMac. In this thesis, a complete method that both captures the 3D surface deformation of volcanic edifice in analogue modeling, and allows for the intrusion to be excavated is presented. In a real geological setting, this would be the equivalent of eroding away the entire volcanic edifice to see the magmatic plumbing system beneath, in high-speed. Such ancient plumbing systems can be found in many places, for example Ship Rock in New Mexico or the Spanish Peaks in Colorado. Back to the method, the deformation pattern can be compared to the shape of the intrusion, which allows for finding coherence between them. The

future goal will be to compare the datasets to real geodetic data, in order to quantitatively test them.

Chapter 2

Theoretical background - Former work

2.1 Field work - aquiring data

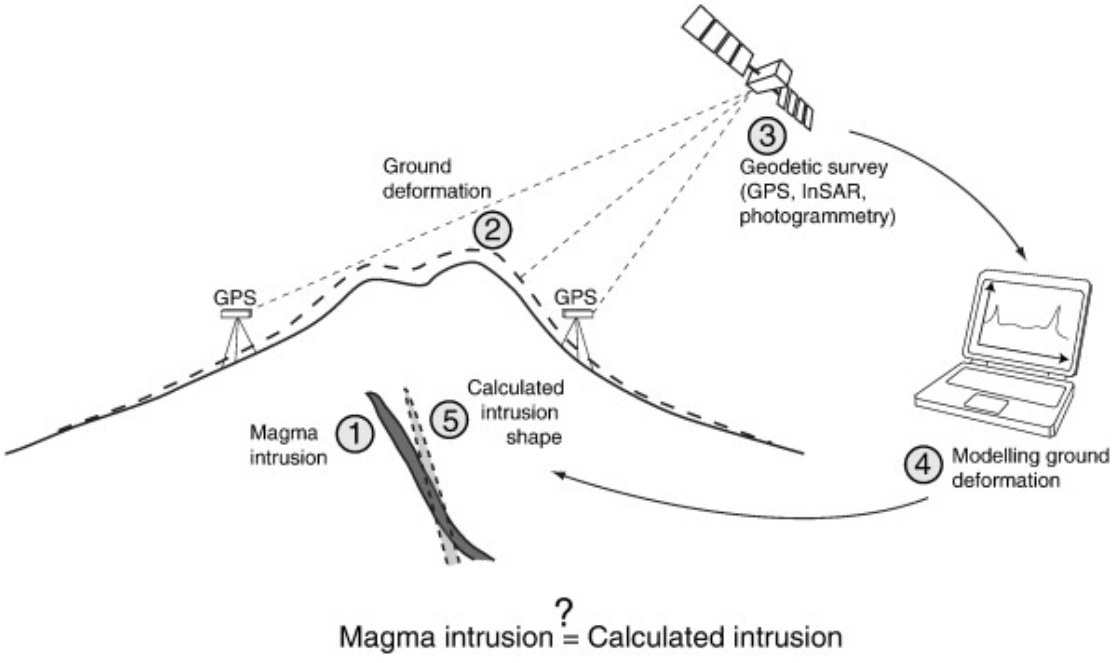

FIGURE 2.1: Schematic diagram illustrating the principle of ground deformation analyses on active volcanoes.Galland (2012)

Volcanoes are often located in remote places and over vast areas up to several hundred square kilometers, making it difficult to monitor their dynamic behavior pre-, during and post eruptive state. The need for remote sensing systems to collect and transmit data over large distances has increased the last decade's (Pedersen and Sigmundsson, 2006). Geodesy is also named geodetics, and is the science of accurately measuring the geometric shape of the Earth, its orientation in space and its gravity field (sensing core curriculum, 2014). Deformation and seismic are the main geophysical methods for constraining the size and shape of magmatic chambers and conduits in addition to monitoring volcanoes(Segall, 2013). Deformation can be measured by several methods, both ground based and space born, and they differ in accessibility and cost. The methods presented here are tilt meter (2.1.1), GPS (2.1.2), aerial photogrammetry (2.1.3) and Inferometric Synthetic Aperture (2.1.4). What they all have in common is their need to make simplifying assumptions of some physical parameters. These are important to remember when processing the data, see section (2.2) about data processing and modeling.

2.1.1 Tiltmeter

Tilt meters have been used to measure surface deformation of volcanoes and couple them to subsurface activity (Battaglia and Bachèlery, 2003; Bonaccorso, 1998; Dzurisin et al., 1983). Tilt meters are carry-on-sized installations that measure the change in slope of the volcano flank. It is a small container filled with a conducting fluid, electronic sensors and a bubble. The electronic sensor registrar the change in the bubbles position and calculates the amount of tilt needed for this movement to happen(**?**). The sensitivity of the method is range from $\sim 10^{-7}$ to $\sim 10^{-9}$ radian (Dzurisin, 2006) depending on the quality and price of the equipment. The use of tilt meters is a less expensive method if compared to other geodetic methods, and the advantage of the method is that it gives continuous, near-real time output data (Battaglia and Bachèlery, 2003) during volcanic activities. Because the data output are directly proportionate to the tilt of the volcanic flank, it does not need heavy data processing such as other geodetic methods, and the data can be analyzed while the event is ongoing. The disadvantages with the method are that the installations need to be set up and they also require maintenance, and there is a possibility for damages by impact from erupted volcanic products (Dzurisin, 2006).

2.1.2 GPS

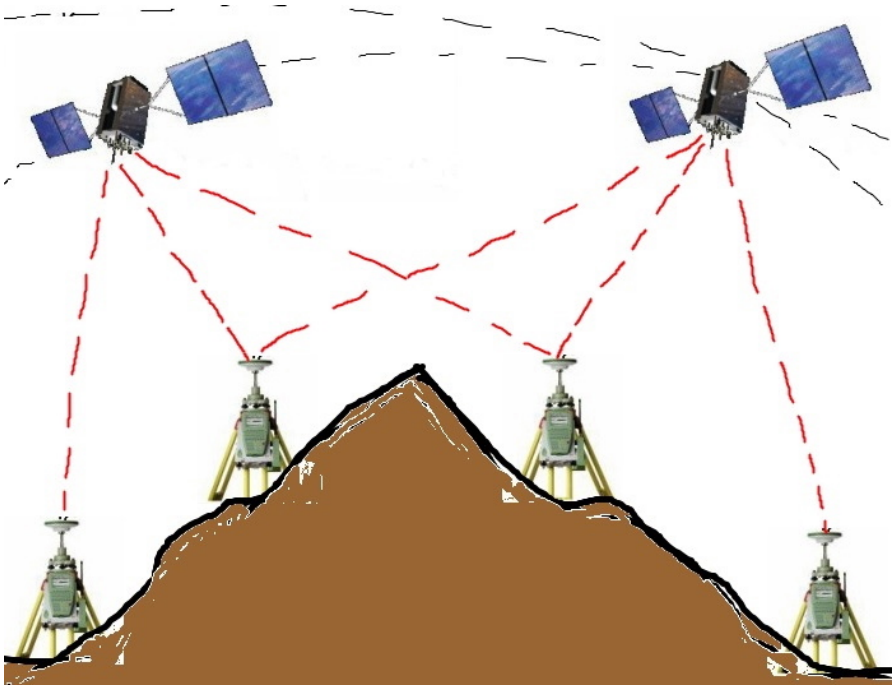

FIGURE 2.2: Simplified graphic explanation of GPS geodetic surveillance acquisition on a volcano. Monitors are found both at the flank close to the peak and at the flat ground surrounding the volcano. The GPS close to the summit detect deformation of the flanks, while the GPS monitors surrounding the volcano can be used to confine the size and the location of the magmatic body. The red dots represent the signal from the satellite to the GPS receiver, the black dotted line represents the route of the satellite, and the black line represents the baseline in-between the GPS receivers.

GPS is a widely used method for monitoring surface deformation at volcanoes (Aoki et al., 2013; Burchardt et al., 2010; Owen et al., 2000; Segall and Davis, 1997; Sigmundsson et al., 1992, 2010; Sturkell et al., 2006). GPS is an acronym for Global Positioning System and is a space based satellite navigation system that measures the accurate change in latitude and elevation pr. time unit at the ground based receiver's position. It has a range between 0 to hundreds of kilometers Cecchi et al. (2003). The Global positioning system includes 24 satellites (Segall and Davis, 1997), where each of them orbits the earth twice a day, and can determine receivers positions to less than a cm (Segall, 2013). This continuous measurement gives the GPS a high temporal resolution, which is necessary when monitoring surfaces that constantly change. A GPS monitor is normally within the range of four satellites, where the more satellites that can confirm its position, the more accurate

the measurements are. GPS satellites continuously transmit an estimate of the satellites position, and it gives both vertical and horizontal measurements which gives a more robust data. GPS is different from other geodetic techniques that instead of measuring only its position relative to two points, it measures its position in 3 dimensions relative to a fixed absolute reference frame (Dzurisin, 2006; Segall, 2013; Sigmundsson et al., 2010). When using GPS to measure surface deformation, the GPS stations movement relative to each other gives away if there is inflation or deflation. Baseline contraction between two stations indicates a deflation of the surface and can indicate magma transport down towards the deep, while baseline extension indicates inflation (Aoki et al., 2013). Inflation and deflation can both be due to transport of magma, but be aware that it can also indicate other factors such as increase in gas/degassing or physical alteration of the magma volatiles (Segall, 2013).

2.1.3 Aerial Photogrammetry

Photogrammetry is the method of comparing two topographic maps from two different times made of high-resolution photos with a high percentage overlap to find the surface deformation. Aerial photogrammetry is the method of capturing these images using aerial cameras. It was used to monitor the development of the Mount St. Helens in 1980 (Jordan and Kieffer, 1981; Moore and Albee, 1981), and the Piton de la Fournaise volcano, in The Reunion Island (Cayol and Cornet, 1998). Cameras used for the acquisition are classified as film (Cayol and Cornet, 1998) or as digital(Pesci et al., 2007). Aerial Photogrammetry is a repeat survey method, with a footprint range of tens of meters to tens of kilometers and a precision of dm to cm scale (Cecchi et al., 2003). The high-resolution images requires a minimum 60 % overlap by preceding image and 25 % overlap laterally, see fig. 2.3.

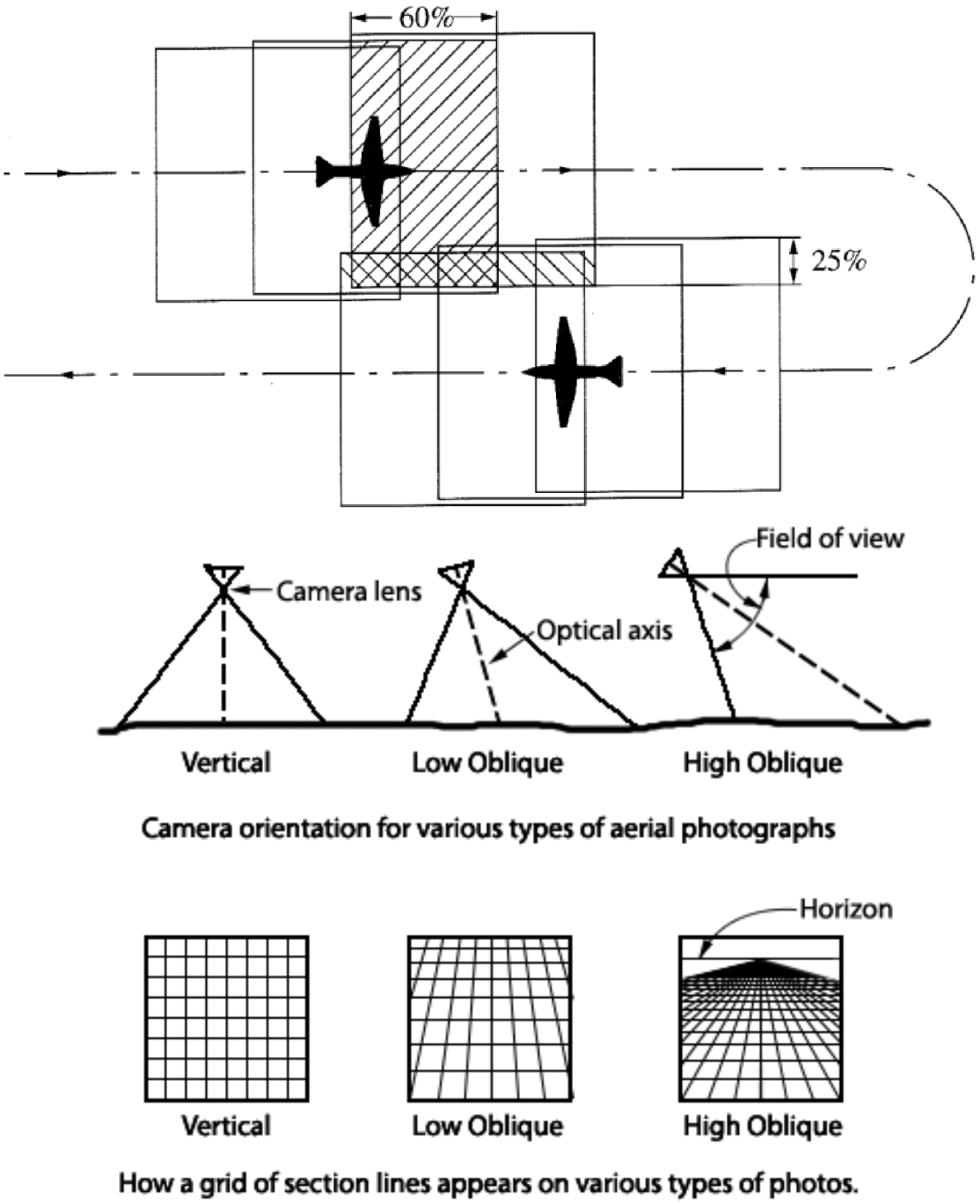

FIGURE 2.3: Figures displaying the method of photogrammetry used on active volcanoes. Right: The flight tracks need a minimum of 25% overlap with 60 % overlap within the successive photos. Reuter (2014). Left: View of camera lens: vertical, oblique and high oblique. (DeWitt and Wolf, 2000).

2.1.4 InSAR

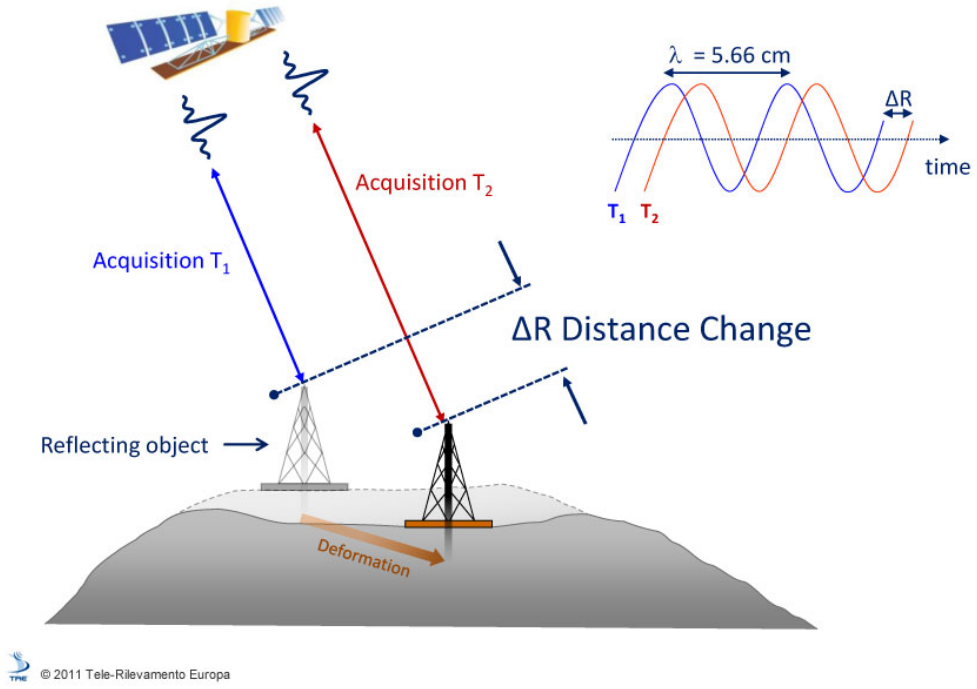

FIGURE 2.4: Interferometry Synthetic Aperture radar. Acquisition 1 is before deformation and Acquisition 2 is after. The phase change is graphically described in the upper right corner, where δR is the change between T1 and T2.Tele-Rilevamento-Europa (2014)

Interferometric Synthetic Aperture (InSAR) is becoming an important tool for volcanologists and geoscientists around the world, because of its ability to measure surface deformation on volcanoes with high spatial resolution (Segall, 2013) in remote and inaccessible places (Ebmeier et al., 2013; Pedersen and Sigmundsson, 2006; Pyle et al., 2013; Wauthier et al., 2013). InSAR is a repeat-survey satellite or aircraft based radar technique that can measure ground deformation down to cm scale (Amelung et al., 2000; Ebmeier et al., 2013; Pyle et al., 2013) and are the methods of measuring the change in phases between two signals over time (Tele-Rilevamento-Europa, 2014). Radar signals are sent from satellites rotating around the earth (2.4). When the signal hits the ground at some point, it is reflected back to the satellite, which record the two-way travel time from the satellite, the phase of the signal and the angle of incidence to the ground. Figure 2.4 illustrates the method of acquisition of the signals T1 and T2, and the relationship between the ground movement, ΔR, and the change in this signal phase, α.

2.2 Data processing and modelling

After the acquisition through either of the methods described above, the data needs to be processed and all the simplifying assumptions need to be accounted for.

2.2.1 Processing the data

Tiltmeter

As mentioned before, tilt meter data does not need advanced processing since its movement is directly perpendicular to the ground. But according to Harrison (1976) tilt meters are susceptible to affects produced by the local topography such as cavities, and by high temperatures from heat exchange in the ground (Bonaccorso, 1998).

GPS

Since GPS acquisition can be either continuous or repeat-survey it needs to be processed differently depending on the temporal scale it covers. The GPS signal is usually averaged for 24 hours if the deformation is small (Larson et al., 2010), but when the deformations are large then it can be necessary to have hourly measurements, such as in Owen et al. (2000) and Segall et al. (2001). The signal is affected by both atmospheric and local conditions: 1) local environmental changes in temperature depending on the time of day and season, 2) weather impacts such as heavy precipitation that causes surface loading and 3), both water vapor in the atmosphere and snow accumulation on the GPS antenna can create phase shifts (Dzurisin, 2006; Larson et al., 2010). The signals also need to be corrected for multipaths, which is when the signal is obstructed in its way from the satellite to the GPS receiver and is reflected. Then the signal ends up with a longer signal path than necessary.

Photogrammetry

Low flight height and high relief such as steep volcanic flanks, gives high distortions for high quality images. By rectification of the images, e.g. creating an ortho photo, this distortion is removed. The objective of compiling an ortho photo is to obtain the 2D image information. For full 3D information, a stereo model is needed. Before either of these can be compiled, the orientation of the images

needs to be performed in these three steps: 1) interior orientation, 2) relative orientation and 3) absolute orientation (Dzurisin, 2006). The minimum GCPs needed to orientate the stereo model is 5 points: 2 horizontal (x,y) and 3 elevation points (z).

InSAR

From figure 2.4, the distance between the sensor and the point will change if the ground have deformed in-between the times of acquisition and this causes a shift in ΔR between T1 and T2. From Tele-Rilevamento-Europa (2014) the change in signal phase ($\Delta\varphi$) can be expressed as

$$\Delta\varphi = \frac{4\pi}{\lambda}\delta R + \alpha + t + noise \tag{2.1}$$

where λ is the wavelength, δR is the displacement and α is the phase shift due to different atmospheric conditions at the time of two radar acquisitions, t is the topographic distortions arising from slightly different viewing angles of the two satellites and noise are the combined effects from de correlation sources. The signal phase is also affected by atmospheric effects such as altering of the wavelength when the signal travels through an atmospheric layer with high moisture content and range displacement, δR, that occurs when the distance between the sensor and the point of interest have changed.

2.2.2 3D displacement

GPS

For finding the 3D displacement, the GPS data separates between the horizontal and the vertical displacement. The baseline extension, which is the distance between two GPS receivers on the ground, is used for measuring the displacement. If the baseline extension increases, then the distance between the stations increase and you have uplift. If the baseline extension contracts, then the distance between the stations decrease and you have deflation. The data is stored as 3 dimensional coordinates in a relative coordinate system and the 3D displacement can be extracted by extracting the difference between the two acquisitions. The displacement is often modeled with vectors displaying the size and direction.

Photogrammetry

For finding the 3D deformation in-between two repeat surveys using the high-resolution images, there is a 3-step process. 1) create ortho photos for finding the flat topography, 2) create a point cloud file for finding the elevation and 3) create a digital elevation model (DEM) using the data from the two latter steps. Then compare two time steps and derive the 3D deformation.

InSAR

For finding the 3D deformation using InSAR is similar to photogrammetry, and is done by comparing two inferferograms. According to Massonnet and Feigl (1998), an interferogram from a two-pass interferometry are computed in 5 steps;
1) Coregistrering, using a correlating process to obtain the offset and the difference in geometry between the two images which are either complex, high resolution images or raw data (Dzurisin, 2006). 2) One of the radar images must be registered with absolute geographical coordinates , 3) then a topographic filter is added in-between the two radar images when they are compiled, to account for geographical features such as steep reliefs. 4) Eliminating the topographical effects by subtracting the fringes created by the DEM and then 5), the interferogram is projected in to a real geographical coordinate system.

When the 3D deformation pattern has been acquired, then the next is to find the best fit for the different parameters. This is done by using geodetic models to test different shapes of the source to fit the deformation pattern.

2.2.3 Geodetic models

Given some preceding assumptions, geodetic inverse modeling may provide information about the shape, size and evolution of the magma plumbing system, in addition to the propagation of sub surface magma transfer (Pedersen and Sigmundsson, 2006). Some of these models that have been developed, are more frequently applied (Cayol and Cornet, 1997); The Mogi (1958) model is a theory that gives an analytic solution for surface deformation due to a point source in elastic half-space. It is a simple model that gives the relationship between the deep magma body with spherical shape and the measured dome at the surface, with the assumption that the size of the sphere is small compared to the depth of its burial.

Dieterich and Decker (1975) used finite element modeling to compute vertical and horizontal surface deformations for various shapes of idealized magma reservoirs, such as dikes, vertical plugs, spheres, sills and horizontal lenses.
Okada (1985) analytical expression defines the surface deformation for a finite rectangular source in elastic half-space. The source is defined as a dislocation, and can for example be tectonic faults or volcanic dikes. The elastic half space is the representative for the Earths crust in a mathematical model. It is an ideal, semi-infinite elastic body modeled by half a sphere, where the ground is mechanically isotropic and the material is homogenic (Dzurisin, 2006).

2.2.4 What is missing?

The whole process of acquisition, analyzing and modelling the data contains several steps of assumptions, corrections and interpretations. In addition, these models does not account for a dynamic, heterogenic system, but assumes that the bulk mass is homogenous, mechanically isotropic and that the magma doesn't interact with the host rock in terms of thermally or chemically reactions. These methods require simplifying assumptions, post-data processing and then modeling by using the best fit. We can't quantitatively test the geodetic models without physically entering the plumbing systems of the volcano! To overcome these limitations, we need to use a physical system, in which (1) both surface deformation and the shape of, and pressure in, the underlying conduit are known, and (2) the mechanical properties of the host material are controlled and well known.

2.3 Laboratory experiments

It is important to remember that in analogue models, there are simplified conditions as well. The materials used in the experiment have to be properly scaled as it needs to be geometrically, kinematically and dynamically comparable with its natural geological model (Galland et al., 2006). If the materials and dimensions are properly scaled down, then the geological processes can be reproduced in a smaller, manageable size and in a recordable timescale (Galland et al., 2006). The constant viscosity and pumping rate of the fluid makes the deformation by fracturing much easier, and you avoid marginal cooling along the edge of the intrusion

(Merle and Vendeville, 1995). There are two ways of designing an experiment where both the surface deformation and the shape of the intrusion are acquired : 1) A sheer model where the intrusive system can be observed during and after the experiment, or 2) a model where the intrusion can be excavated after the experiment. These two experimental ways depends on the properties of the materials that are used for crust and magma.

2.3.1 Crustal analogues

Previous experiments with analogue models such as mentioned above have been performed. For the first type, gelatin is the most common material used as elastic, crustal analogue (Hubbert and Willis, 1972; Kavanagh et al., 2006; Rivalta et al., 2005; Takada, 1990, 1994). It has the advantage of a transparent body, giving us the possibility to monitor and document the formation of the magma plumbing system while the experiment is running. Gelatin fails in tension (Hubbert and Willis, 1972), but not in shear, making it unfit to model crustal faulting (Galland et al., 2006).

In the latter type, dry granular materials are the most common. They are more susceptible to alteration of density, and the material can easily be removed when excavating subsurface inclusions. In addition, the materials are known for being good for modeling upper crustal mechanical behavior (Galland et al., 2006; Hubbert and Willis, 1972; Krantz, 1991; Rossi and Storti, 2003; Schellart, 2000; **?**). Of these materials, sand are the most common materials used in analogue modeling, both for modeling faulting (Krantz, 1991), hydraulic fracturing (Hubbert and Willis, 1972), folding (Reber et al., 2013) and of course volcanic deformation (Tortini et al., 2013). Other materials used are flour (Tortini et al., 2013), diatomite (Gressier, 2010) and ignimbrite powder (Mathieu et al., 2008), and silica powder (Galland et al., 2006).

2.3.2 Magma analogues

For the two ways of designing the experiment, the first requires the fluid to be visible through the sheer medium, the latter requires that the liquid to inhabit a solid state in room temperature. Different materials used as magma analogue is silicone (Donnadieu et al., 2003; Merle and Vendeville, 1995; Takada, 1990),

vegetable oil Galland et al. (2006), golden syrup (Abdelmalak et al., 2012; Mathieu et al., 2008), honey (Mathieu et al., 2008), water (Takada, 1990) and linseed oil (Takada, 1990). The vegetable oil is the only one of these materials that solidifies in room temperature.

For the experiments in this procedure we are using crystalline silica flour for crustal analogue, and vegetable oil as magma analogue. The only experiments that produce realistic sheet intrusions are given by these materials. They will be described in chapter 3.1.

2.3.3 Methods used for monitoring surface deformation

Several techniques have been used for monitoring ground deformation in volcanic systems in analogue modeling. Among them is N-view reconstructions (Cecchi et al., 2003), which needs multiple angle view to aquire high reolution images. Laser technologies have been used (Graveleau and Dominguez, 2008; Lague et al., 2003), but they have low resolution and do not not separate horizontal and vertical displacement. Microsoft Kinect sensor is a type of laser (Tortini et al., 2013). Then there is structured light techniques (moiré projection) (Galland, 2012; Galland et al., 2009) which also have been used for modeling the shape of the intrusion. But this method only monitors from a vertical angle, which infers that it can only be used on flat or saucer-shaped intrusions. In addition, does not separate the horizontal and vertical displacement, same as for laser monitoring. The last method is photogrammetry (Delcamp et al., 2008; Donnadieu et al., 2003; Mathieu and van Wyk de Vries, 2011). According to Donnadieu et al. (2003) there have been three successful techniques of digital photogrammetry applied to laboratory analogue models that is used for study surface displacement by volcanic activity. The first is the horizontal side-perspective video, the two others are vertical perspective views, which uses either one single camera (monoscopic) or two cameras (stereoscopic) for multiple view angles.

2.4 What is missing?

The methods presented above do all lack something. Either the resolution that is too low or it is the setup that is too complicated, or even the horizontal and vertical

displacement cannot be separated, there is need for a more complete method. For the experiment, we need a method of monitoring the surface that can give us both horizontal and vertical displacement, separately. The setup needs to give high-resolution data (sub pixel) in addition to be easy to set up, cost-efficient and compatible with the analogue model. For the experiments in this procedure we have chosen the photogrammetric method of stereoscopic angle with multiple photo cameras. This is because it is has proved capable to capture the surface deformation in 3D and provide topographical changes.

Chapter 3

Laboratory volcano geodesy : Experimental procedure

The experimental setup including the materials used in this analogue experiment is presented in chapter 3.1, then the procedure of the experiment in chapter 3.2. This chapter is divided into 5 subchapters explaining the steps of the procedure: The preparation of the experimental box in 3.2.1, compaction of the flour in 3.2.2, the photogrammetric setup for the experiment in 3.2.3, the execution of the experiment in 3.2.4, and then the excavation of the intrusion in 3.2.5. The results of the experiment can be seen in chapter 3.3 where the shapes of different intrusions are displayed. Here, in 3.3.1 is the photogrammetric method for the intrusion explained.

3.1 Experimental setup

This setup is an experimental model used for reproducing realistic sheet intrusions in the laboratory, similar to the real magmatic intrusions found in a volcanic edifice. This setup does not only produce the sheets, but allow for the intrusion to be excavated and for their shape to be modeled in 3D. This is due to the properties of the oil, presented below. All of the experiments were performed with the same parameters.

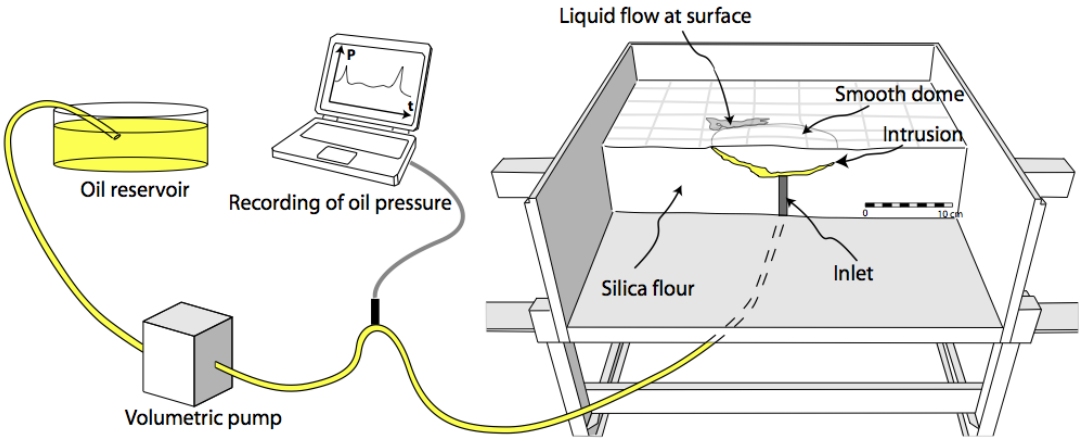

FIGURE 3.1: Experimental setup. The box is connected to the oil via a pump and a pressure gauge. The sketch show the cross section of the box with flour, where the oil is pumped through the inlet where it propagates up towards the surface. (Galland, 2012)

The two materials used in this analogue modeling is 1) a fine-grained flour consisting of crystalline silica and 2) a molten, low viscosity vegetable oil. The scaling properties of these materials were presented in Galland et al. (2006).

The crystalline silica flour (see fig. 3.2) is representing the brittle crust; it fails according to the Coulomb criterion (Galland (2012); Galland et al. (2006, 2009)). The silica powder is fine grained enough ($10 - 20\mu m$) to stop percolation of low viscosity fluids, and it is highly cohesive (angular grains) after compaction (Galland et al. (2006)). By compacting the flour we can control the density, se section 3.2.2. The vegetable oil is representing the low viscous magma and the oil that is used for the experiments is the cooking oil 'Vegetaline', produced by ASTRA. It solidifies at room temperature, making it possible to excavate the intrusion in one piece. Its a Newtonian fluid with a melting temperature of 31 °C. The injection temperature is 50 °C with a viscosity, η, of $2 * 10^{-2}$Pa s.

The experimental setup used in this thesis was developed by Galland et al. (2003) and later modified in Galland et al. (2007, 2009) and Galland (2012). The materials in the experiment were presented in Galland et al. (2006).

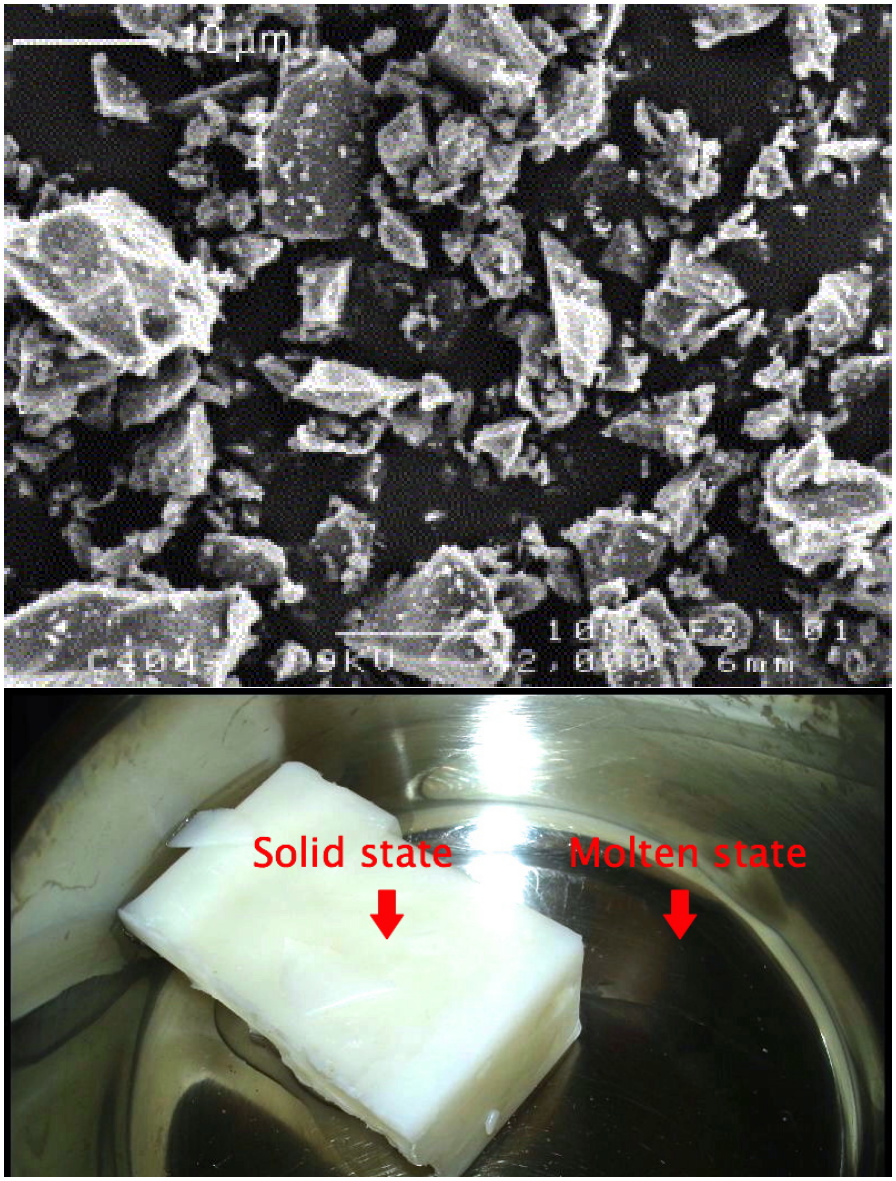

FIGURE 3.2: The materials used in this experimental setup. Above: Scanning Electron Micrograph of crystalline silicapowder with angular grains (Galland et al., 2006). The white bar gives scale. Below: Vegetaline vegetable oil in solid and molten state.

3.2 The procedure of the experiment

This chapter is divided into 3 parts:
1) The compilation of the box and the preparation of the flour, 2) The photogrammetry setup and the experiment, and 3) the excavation and documentation of the intrusion.

FIGURE 3.3: Introducing experimental procedure.

3.2.1 Initial preparations

The setup is graphically explained in figure 3.1. The model is placed in a square box, that measures $40 * 40$cm, where the height can be varied. In the bottom center of the box there is a fixed circular inlet pipe in metal with height of 6 cm, inner diameter of 5mm. This is used when pumping the oil into the flour. The steps for assembling the box are presented below.

(B : steps for assembling the box)

B1. Plug in the contact for the melting plate to melt the oil.
B2. Create a plug for the metal pipe by using metal thread and paper, and dip it in oil. The oil will solidify within the pipe, and keep the flour from filling up the pipe during the compaction later on.
B3. Now, assemble the box. It consists of two loose walls, for each of them 4 small screws and 2 or 3 large screws. Tighten them well, but carefully to avoid loosening during the shaking. There should be no gaps in-between the fiberglass and the metal floor of the box.
B4. Add the number of fiberglass levels on the box to achieve the desired height. The screws that keep the additions together needs to face the same way as the original box. This is necessary when wanting to disassemble the box before excavation. The upper level is the one with a smooth surface on the one side.
B5. Move the large fiberglass cage over the box with the doors facing towards you. Use a table with wheels for transportation.
B6. Connect the shaker to the metal inlet of the box, and fasten the screws. It needs to be tightened very well to avoid it falling off when shaking. Remember to check which way the shaker is fastened; it determines the direction of the compaction and the orientation of the flour grains.
B7. Attach the clamps at each corner of the box, and tighten them bit-by-bit to secure an equal compression of the sides of the box, and avoid skewing.
B8. Put paper in the bottom of the safety box, and use a syringe to soak it with water. This is to fix the excess flour that escapes from the box.
B9. Open the window and let the end of the air fan out. Turn it on by plugging in the outlet, and check the direction of the airflow by holding a paper in front of the tube. Place the end of the tube over the cage; the opening should be horizontally aligned with the top of the box.

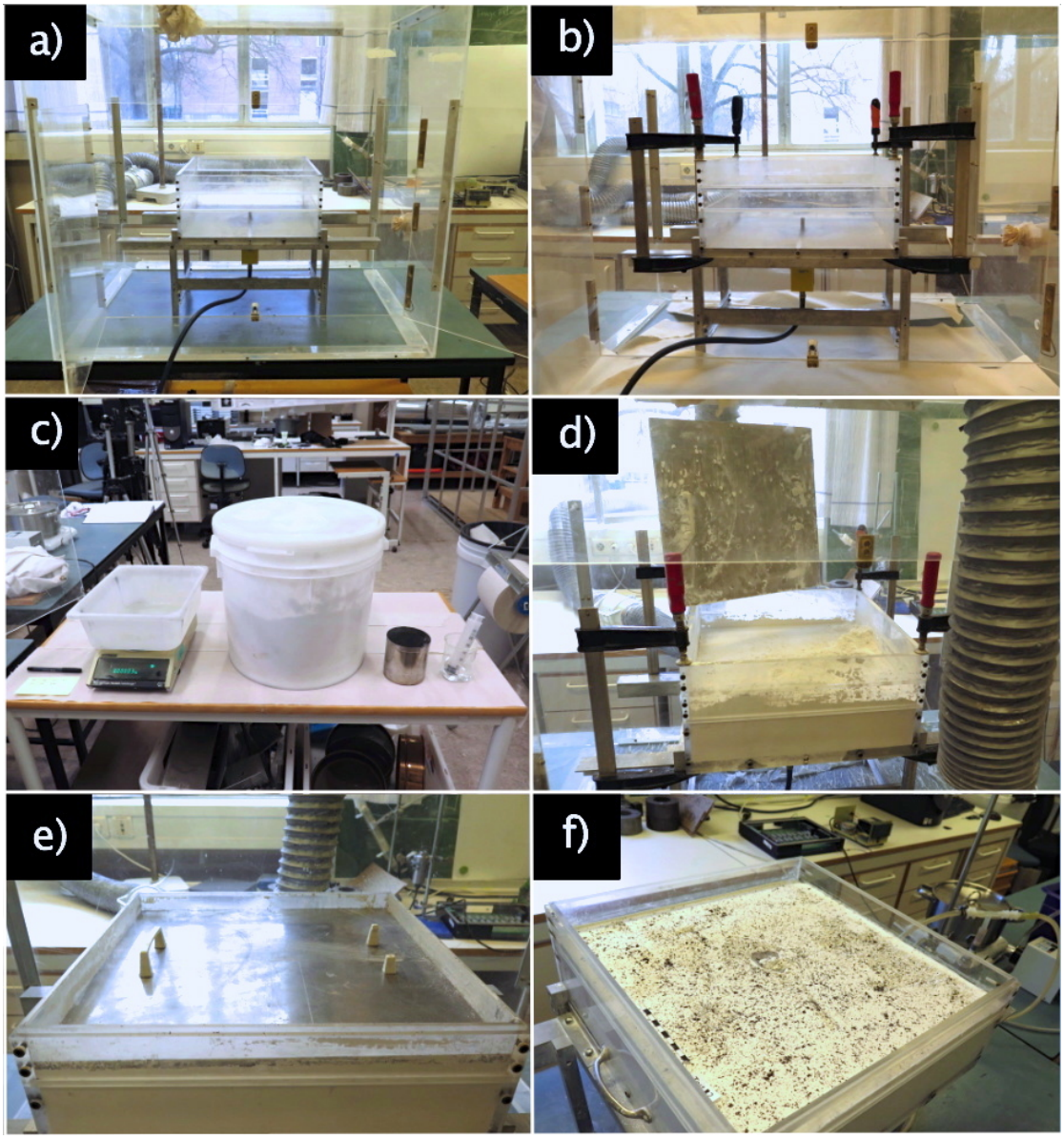

FIGURE 3.4: Compiling the box with the flour. **a.** The box inside the safety cage. The shaker is attached. **b.** Clamps attached. **c.** Table with flour and weight. **d.** Preparing the flour for compaction. **e.** After compaction, before preparation of surface. **f.** Model is ready for experiment. The surface contrast is enhanced with small coffee grains evenly distributed.

3.2.2 Flour Compaction

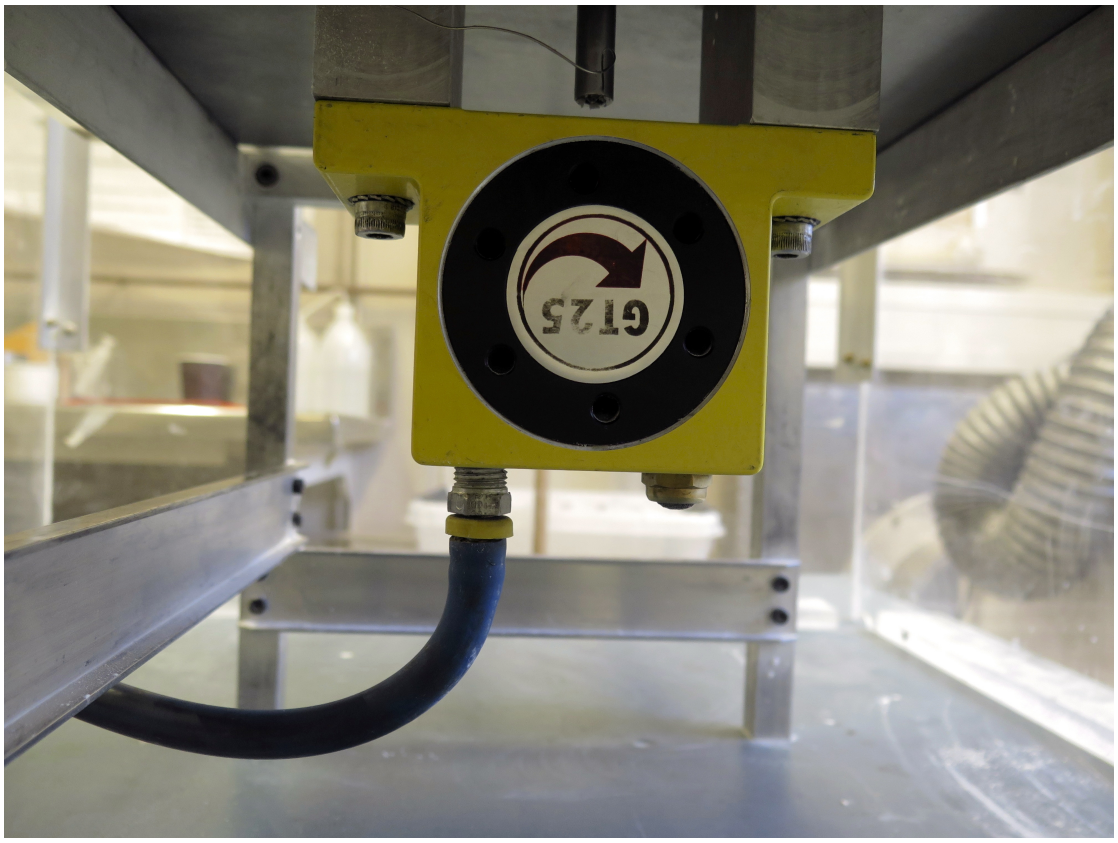

FIGURE 3.5: High frequency compressed air shaker attached to the bottom of the model. The arrow points to the direction of the vibrations; clockwise from the pressure inlet.

One of the most critical parameters for controlling the experiment is the density. By compacting the flour, we can control its density. Here, we compact it to the optimal density of $1{,}05g\ cm^{-3}$ and thereby increasing the cohesion by 3 times (From Galland et al. (2006): before compaction: C $\approx$ 100 Pa, while compacted C $\approx$ 300 Pa.)

Since the dimensions of the box is know, in addition to the mass of flour and the thickness of the metal plate used for compacting, then we can calculate the height of the flour needed for achieving the optimal density.

The compaction is performed by using a high frequency compressed-air shaker (See fig. 3.5: Huston Vibrator model GT-25). The air shaker compacts by vibration, which make the flour act as a fluid, flowing in the direction that the air is pumped. The maximum density of the flour is a time dependent parameter, since the degree of compaction is determined by the amount of time spent on vibrating.

The compaction is explained in the steps below. (F = steps for preparing the flour)

F1. Find the excel file used to calculate the mass of silica flour which is needed. This program will be used to calculate the density after each shaking. See example in appendix A.
F2. Move the rolling table up next to the cage, and place it perpendicular to the short side. Cover it with paper, and place the box of flour on top.
F3. Place the scale in-between the flour box and the cage and connect the power outlet and place the small white box on top of the scale. The scale should be in kg mode, and rebooted after the white box is placed on top.
F4. Put on a lab coat and a mask for lab safety.
F5. Measure the flour in 2.5 kg segments at the time, and keep track of how many of them you have added to the box. While measuring, hold the fan close to the flour to suck up suspended flour particles in the air. Pour the flour carefully in the box, away from the opening.
F6. When all the flour desired is measured and put in the box; remove the flour box and the scale. Move away the rolling table.
F7. Flatten the surface of the flour with a spatula, and place the metal plate on top. The plate should be as horizontal as possible, so apply pressure on the plate with you hands, carefully, until this is achieved.
F8. Use the precise ruler to measure the height of each corner. Enter the numbers in the excel file to find the density. The optimal density used in these experiments were 1050 $kg\ m^{-3}$.
F9. Turn on the air pressure and increase to 2.2 bar in the pressure gauge.
F10. Start the shaking when you are ready. Control the time using a stopwatch. Make sure the surface is horizontal through out the shaking by placing the spirit level on top.
F11. When the time is up, stop the shaker. Repeat step **F8.** and compare density to other experiments. Check the differences in height to ensure horizontal surface.
F12. Carefully remove the metal plate, shake of the excess flour into the box and use the spatula to even out the surface again. Put the plate back on top.
F13. Repeat step **F9 - F12** until you have the optimal density.
F14. Repeat step **F12.** and run the compacter for 5 seconds to ensure optimal horizontality. Leave the metal plate on top of the flour.
F15. Turn of air pressure. Remove the shaker from beneath the box. Screw of the all clamps carefully, bit by bit, to prevent skewing. Remove the excess fiberglass

levels of the box.

F16. Turn of the fan and remove it. Remove the safety box by using the rolling table.

Remove the metal plate carefully and add grained coffee beans (smallest grains possible). This is to create texture in the white flour, which is needed by the computational analysis for optimal particle tracking. Place the metal plate on top and "knock" carefully to remove any surface elevation. Remove the metal plate. Put in a scale and label of the experiment in-between corner 1 and 2. The model should now look like `f)` in figure 3.4. Place the wooden plate on the edges of the box .

3.2.3 Photogrammetry setup

The photogrammetry method is using 4 cameras, which are simultaneously triggered by remote controls, continuously during the experiment, to capture the changing surface of the model. The steps for preparing this setup are listed below.

(P : steps for photogrammetric setup)

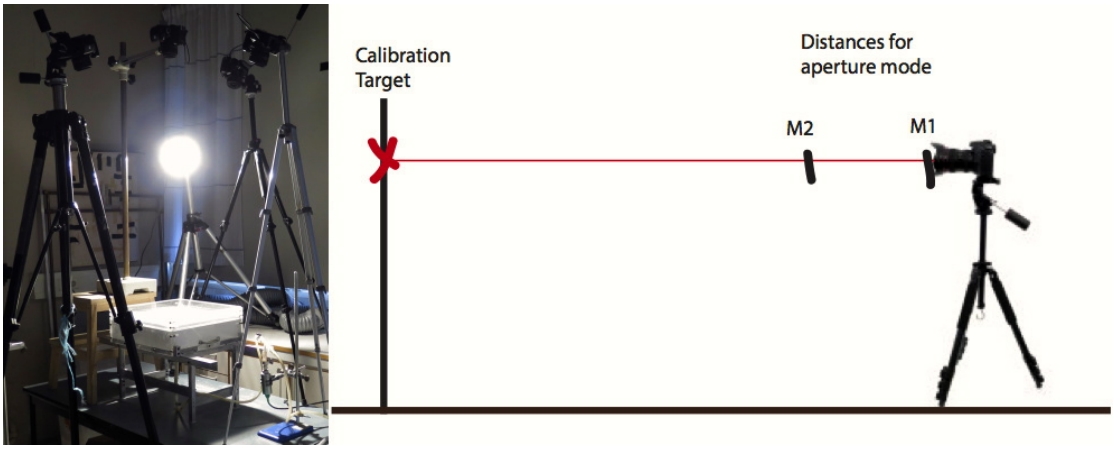

FIGURE 3.6: Photogrammetry setup. Right: displays the distance from the camera lens to the fixed target, when preparing the cameras for the experiment. M1 is the distance from the lens to the model surface, and M2 is the distance from the lens to the center of the wooden plate. Left: The final setup, using four cameras recording from 4 different angles. The roof light has been switched off and replaced by a constant light source.

P1. Prepare the cameras using a heavy tripod; this will prevent the camera from moving and the focus from being distorted. The camera properties are presented below. Use a stick for measuring the distance between the camera and the target, and mark the length on the stick (M1). Measure the distance from the flour up to the top of the wooden plate, and mark this distance (M2) on the stick from M1 towards the end of the stick. Check the cameras: if they are fully charged. Check the remote controls if they have new batteries.
P2. Number the corners of the box, and stick to this throughout the experiment and the analysis.
P3. You need three tripods and one heavy stand with a horizontal prolonger. Place the heavy stand on the side where you have corner 1 and 2. The other tripods can be placed in either of the sides of the box, depending on their length, if they must stand on the floor or not.
P4. The cameras are numbered, so they must always be placed in the same order. Camera 1 on the heavy stand, camera 2 between corner 2 and 3, camera 3 between corner 3 and 4, and camera 4 between corner 4 and 1. Check that the distance from the cameras to the center of the wooden plate match the distance of M2.
P5. Place a 5.th tripod close to the experiment, and attach a continuous light source (LED), which is directed oblique at the box, as seen to the left in figure 3.6. The LED lamp is placed in front of the box to control the light settings and avoid affects from the flickering fluorescent lamps in the roof.
P6. Close the curtains to prevent daylight from affecting the results.

The cameras used in these experiments are four NIKON D3200, each with a remote control receiver. Attach the remote control to the camera, and place the tripod in front of the target with the distance M1 between the lens and the point (see fig. 3.6). Here M1 is 112.0 cm and M2 is 23.0 cm. The camera is set in mode A, where the aperture can be controlled, here: 14. The lens must be in semi-automatic mode, and choose the AF mode to be single point. Check if the remote control works from different angles. Then switch the lens to manual mode. The aperture is now fixed.

3.2.4 Performing the experiment

The purpose of performing the experiment is to recreate the mechanics behind the emplacement of an igneous intrusion in a volcanic edifice, and to monitor the surface while this is happening. The oil, representing the magma, is pumped from the pan, through the pipes and in to the model via the inlet. While the oil propagates through the flour, the surface of the model deforms by doming. The steps for performing the experiment are presented below.

(E : steps for the experimental part)

E1. Pull the plug from the metal inlet!
E2. Check the pressure gauge: power on, height over table, horizontality.
E3. Open up Labview with the program that controls the pressure and the triggering of the cameras.
E4. Couple together the tubes in the setup as seen in figure 3.1. In-between the pump and the pressure gauge, there is attached a valve with three outlets. Attach the inlet tube to the inlet pipe.
E5. Run a test of the pressure without the cameras being connected. This is for measuring the atmospheric pressure. Then fill the T-pipe with water, which will prevent the oil from entering the pressure gauge, and run another test. Save this as 'pressure test with water'. Height of pressure gauge used in these experiments was 34,2 cm.
E6. Fill up a bucket with hot water and attach it to one of the outlets of the valve. Switch the valve so that the oil will be flowing through the whole system, isolated from the water bucket.
E7. Turn on the cameras, turn on the remote controls and test if all setups respond by using the IR sender that is connected to the circuit board (fig. 3.7). Test run LabView to see if all the cameras work.
E8. Remove the wooden plate. Create a continuous flow of oil in the tube (with a flow rate of 40 $ml\ m^{-3}$) by injecting oil into the pipe and hold both ends of the pipe in the oil.
E9. When the tube is filled with oil, and free for large bubbles, then stop the pump and connect the pipe to the inlet of the box.
E10. Turn on the lamp on the tripod and switch of the roof light. The setup should now look like the setup in image 3.6.
E11. OBS!! Now the experiment starts!! Start the Labview program, and

pay attention to the camera sounds. (If they are not synchronized, then stop LabView and check what is wrong.)

E12. Start the pump and the timer, and then put your hand over the model to mark the start of the experiment in one of the images.

E13. Pay attention to the flow of the oil, the changing surface of the model and the camera sounds.

E14. When the oil propagates through the surface of the model, then switch the valve to isolate the experiment from the pan, creating a flow from the pan to the water bucket.

E15. Stop the pump and the Labview program in this order.

E16. Move the tube from the pan to the water bucket and start the pump again, creating a flow of water from the bucket through the pump and back.

E17. Turn of the cameras. After some minutes, stop the pump and leave the experiment for 40 minutes. This is for the oil to solidify.

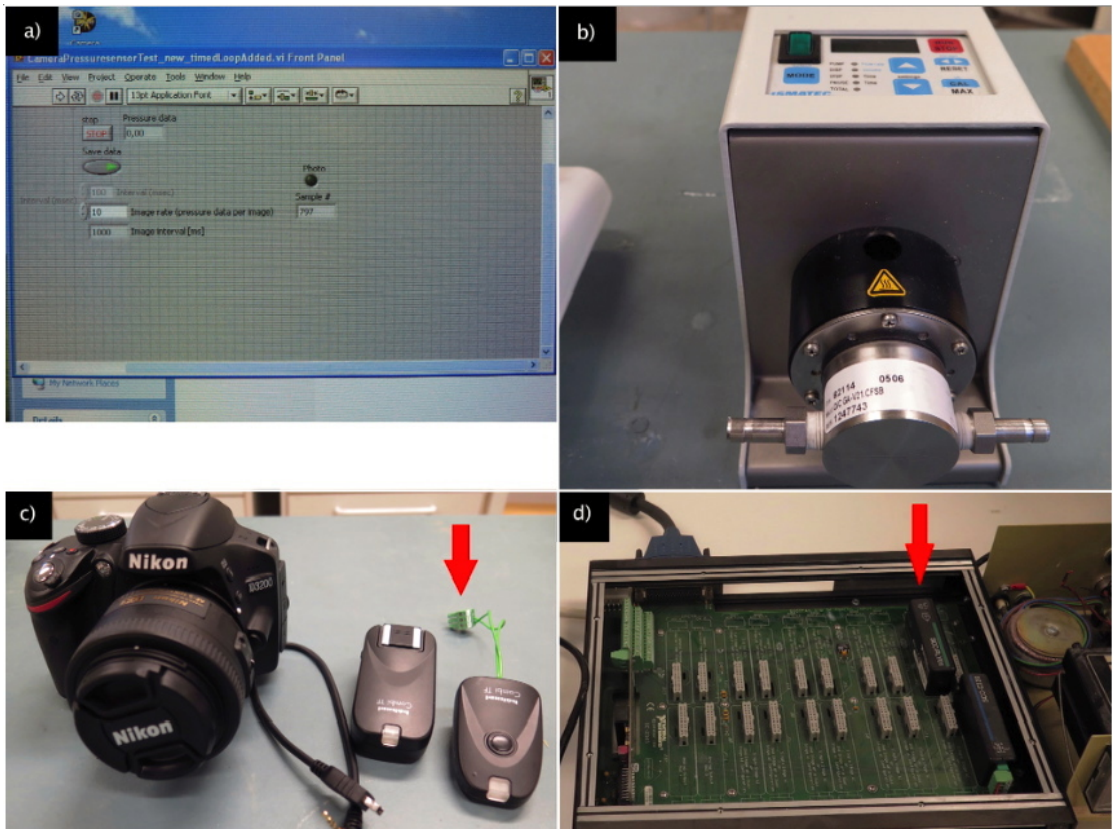

FIGURE 3.7: Final check for the experiment. **a.** Labview used for triggering the cameras and the pressure measurements simultaneously. **b.** The pump transports the oil from the pan to the inlet. The pumping rate was ~ 40 ml pr min. **c.** The remote control set. One is attached to the camera and the other is attached to **d.** the circuit board. This connects the computer to the cameras and the pressure gauge.

3.2.5 Excavating the intrusion

To be able to see the intrusion and to document it, we need to remove the overlying soil. The oil takes about 40 minutes to solidify within the flour, depending on the temperature in the room and the amount of oil that it consist of. The length of the experiment, from the pump was initiated to the oil penetrated the surface, is often a clue to the amount of oil stored within the subsurface. The steps for excavating the intrusions are listed below.

(I : steps for excavating the intrusion)

After the oil solidifies, the intrusion can be excavated. These are the steps to how it can be carefully treated:
I1. Start by moving the table with the box to the middle of the room. This is for the dynamic photogrammetry method later. Put on a lab coat and mask.
I2. Place the cage over the box and prepare the ventilation tube. Repeat step B8 and F2.
I3. Take two medium sized open plastic boxes and place in-between the opening of the cage and the box. These are for catching the falling flour.
I4. Use the spatula and carefully remove the upper surface layer of coffee beans. Throw this in the garbage bin.
I5. Screw off the sides of the box that is faced towards you.
I6. Use the large brush to find the intrusion, carefully, and then use the small brush for excavating it. The spatula is used for removing the flour around the intrusion. All of the flour is going back into the flour bin.
I7. Use the fan actively to remove silica dust from the digging.
I8. When the intrusion is successfully excavated, use a syringe with water to cleanse the intrusion for the excess flour.
I9. Remove the cage and the fan; clean up the table around the box and screw off the rest of the fiberglass walls of the box.

The excavation process can be seen in figure 3.8.

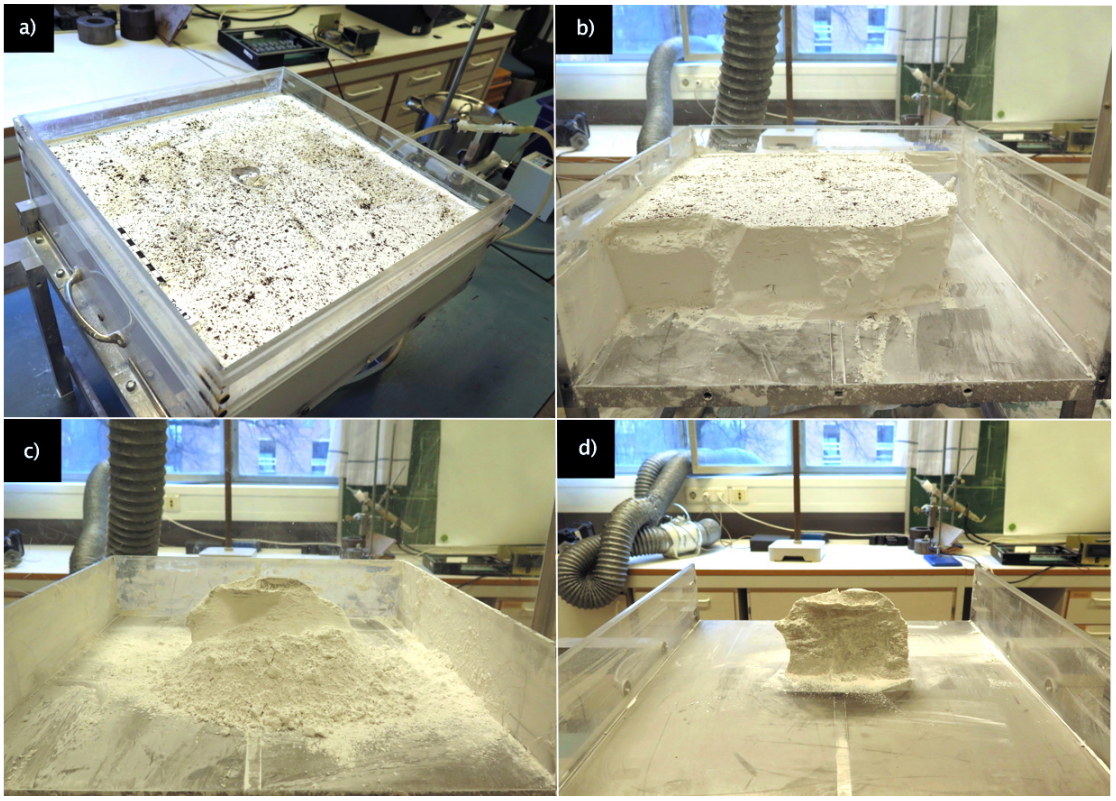

FIGURE 3.8: Excavating the intrusion. **a.** The surface after the experiment. **b.** Carefully removing the flour around the intrusion. **c.** Using a small brush to remove the flour covering the intrusion. **d.** When the full shape of the intrusion is revealed, water is used for cleaning the intrusion for excess flour.

3.3 Intrusion shapes

The shapes of the intrusions in the experiments were all sheeted dikes, but they had different sizes and shapes. In these images, the extrusions had been removed in all but exp. 2 (figure `a)` in 3.9), where the small cone sheet feature on top was the extrusive part. The similar feature in figure `d)` is a subsurface cone sheet. Intrusion `b)` and `c)` are more rounded, bended dikes, with some flat, sill-like appendix appearing close to the surface.

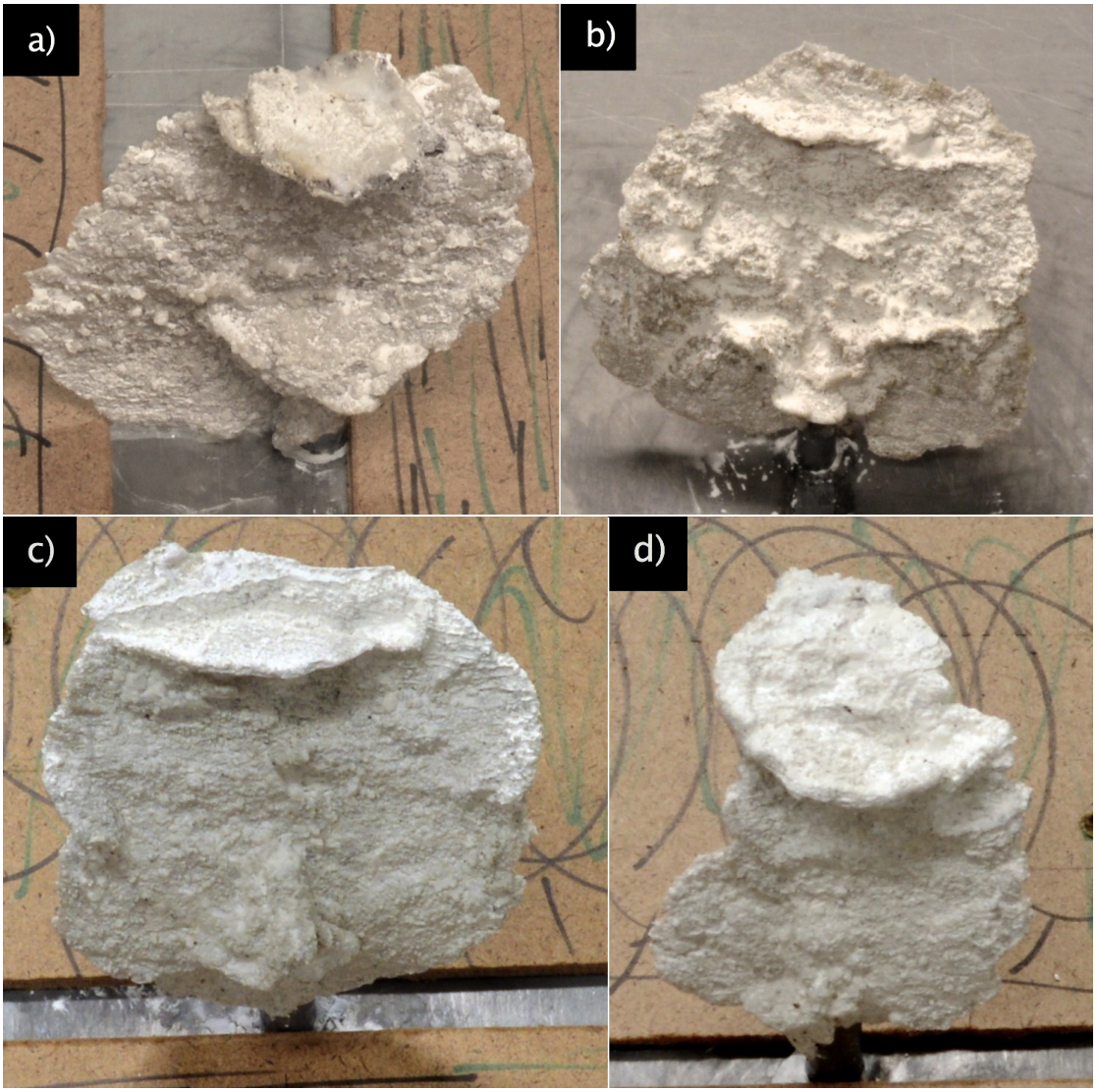

FIGURE 3.9: The intrusions from experiment 2, 3, 5 and 6. **a.** Intrusion from experiment 2. **b.** Intrusion from experiment 3. **c.** Intrusion from experiment 5. **d.** Intrusion from experiment 6.

3.3.1 Photogrammetry method for the intrusion

Explain the photogrammetric method...
(PI : steps for photogrammetric documentation of the intrusion)

PI1. Place cardboards on the side of the sheer parts of the box and on the bottom of the model surface; beneath the intrusion. This is a step that prepares the images for photogrammetric analysis. It is applied to remove reflection from any surface and to prevent the cameras from seeing through the sheer walls.
PI2. Place one camera right above the model with distance M1 (fig.3.6) to the top of the intrusion, normal to the surface of the box. Take one image using the remote control to avoid any shaking of the camera that can cause blurring of the image. The overview images is for geo referencing the model box and to constrain the size of it, while the lower images are for computing the shape of the intrusion.
PI3. Place the tripod with the camera on one of the sides of the box where the wall has been removed. Place it in the same height as the first position, but with a slight oblique view at the intrusion. Remember to have distance M1 between the camera lens and the focus point at a specific point on the intrusion.
PI4. Lower the camera with 10-20 cm, fix the focus point at the same place, keep the correct distance from lens to point and take a picture using the remote control.
PI5. Repeat step **PI4.** until the camera is horizontally aligned with the bottom of the box. Take a picture here using the same method as before. This will be the central image when calculating the shape of the intrusion later in the photogrammetric analysis in chapter 4.2.
PI6. Now, use the same method as above for four more photos, two on each side of the central image. But instead of moving vertically, move the camera horizontally to the side, keeping the focal point fixed on the same spot. Make sure that the whole box is in the photo.
PI7. Now you are done with one side of the intrusion. Depending on the shape, you will need to repeat step **PI3. - PI6** for each side of the intrusion.

FIGURE 3.10: Photogrammetric method for intrusion. Images are taken by moving the camera vertically, keeping a constant distance between the lens and a fixed point on the object.

Chapter 4

Photogrammetric Analysis of the Laboratory Geodetic Data

In this chapter, we explain the method of analyzing the data that was obtained in the lab. The data contains information about the deforming surface and can be used to compute the 3-dimensional shape of both the surface and the underlying intrusion. From the surface analysis explained in chapter 4.1, we obtain the horizontal and the vertical displacement of the surface, creating the equivalent of the InSAR interferograms (see chapter 2.1.4) that show the displacement over time. The evolutional deformation pattern can then be compared to the 3D shape of the intrusion computed in chapter 4.2 to see if there is any link between them, if a particular shaped intrusion gives a unique deformation pattern at the surface.

4.1 Surface analysis

The goal of the photogrammetric analysis is to find the 3D displacement of the surface by using the images from the photogrammetric method and to compare the surface deformation with the shape of the underlying intrusion.

For the surface analysis there are 4 images for each time step: one angle is normal to the surface of the model, and the three others with oblique angles.

For the photogrammetric analysis, the open source photogrammetric tool 'MicMac' has been used. The workflow is explained in chapter 4.1.1 and the complete

documentation of the tool can be found here: Open source photogrammetry tool of MicMac : http://logiciels.ign.fr/IMG/pdf/docmicmac.pdf .

The Micmac workflow use each of the four images acquired from the experiment, to compute an ortho photo and a 3D point cloud file (file.ply). The point cloud file is geo referenced, which will make it easy to compare the point cloud file of the surface and the intrusion. Ortho photos and point clouds are described in chapter 4.1.2 and 4.1.3.

After the photogrammetric analysis, then the ortho photos and the point cloud files are imported to matlab with the purpose of finding hence the δxδy and δz for each time step. The matlab analysis is explained in chapter 4.1.4.

4.1.1 Micmac workflow : Data production

This analysis is based on:
1) The cameras are stationary; aerial mode, 2) the data is divided into time steps; 3) the surface is flat.

Start with exporting the path of the Micmac directory at the computer. From the experiment, all the images are stored in time steps T, with the 4 images marked with number according to the camera they have been taken with (1-4).

Tapioca:
Starting with the analysis with the Tapioca command which computing the tie points of the four images. Tie points are features that correspond to local contrasts that are automatically computed by Tapioca. By using the term 'All', then you compare for all possible pairs, which is the highest resolution and the most time consuming. For more simple calculations then 'MulScale' can be used. Then choose all the images in the folder (here; T1) by using .*.JPG. The size parameter is used for shrinking images. Here it is set to -1, which gives no shrinking.

Tapas: is used for computing relative orientations of the different cameras. By using 'Fraser', which is a radial model with de centric parameters. It has 12 degrees of freedom. Then use all the images again. Out is the output directory specified, here; Ground.

GCPBascule: Georeferences the images from a relative orientation to a system defined by in Dico-appuis.xml file, using at least 4 ground control points (GCP).

Here the coordinate system is called Terrain-Ground. The GCP of the 4 images are defined within the Measure-Appuis.xml: using the pixel at the corners of the box. This is a bit different when orienting the intrusion, see explanation in 'GCPBascule' under 'MicMac analysis of intrusion'.

Tarama: is used for creating a low resolution image (a mosaic) of the whole area using all the images. This will be used in the next step.

SaisieMasq: uses the mosaic and allows you to define a masque for the area of interest, here; the box, leaving out the surroundings that are found in the images.

Malt: is a simplified version of the Micmac interface, which is used for matching the images as an ortho photo generation, with images that can be described as $Z = f(X, Y)$. This is mainly for flat surfaces. ZoomF gives the final resolution, here; 1. It creates a set of individual images along with their affiliated masque and their incidence image.

Tawny: generates the ortho photo mosaic that was prepared in 'Malt' by merging the images and the masques.

Nuage2Ply: It transforms the depth map into a 3 dimensional point cloud file. Attr stands for the attributed directory and the name for the ply file.

Loop for timesteps: The loop repeats the necessary steps for the rest of the time steps, creating an ortho photo and a ply file for each of them. It uses the masques from time step 1, since the camera positions are stationary, these will be the same in all the photos.

Dico-Appuis.xml

Here, define the coordinate system of the box. The box is square, and measure 40 by 40 cm (400 mm). To avoid having zero in origo, the box is 'placed' further out in the field:

Corner 1; Origo = (10 000, 10 000, 10 000)
Corner 2; End of box in x-direction = (10 400, 10 000, 10 000)
Corner 3; End of box in both directions = (10 400, 10 400, 10 000)
Corner 4; End of box in y-direction = (10 000, 10 400, 10 000)

Because the surface of the flour is considered the surface of the model, then elevation = zero.

Mesure-Appuis.xml

For Mesure-Appuis, define the pixel coordinate (x,y) of each GCP. Use a program such as Adobe Illustrator or Photoshop for this.

4.1.2 Output 1: Orthoimage

An ortho photo, displayed in figure 4.1, is a geometrically corrected aerial photograph where the photo has been projected straight down on the flat surface, removing all topographic distortion (Schuckman, 2014). The photo has a uniform scale, like a map, making it possible to calculate real distances with it. From the ortho photo, δx and δy can be found.
The method used by Micmac is very similar to the method of aero triangulation photogrammetry, where manual 'digitizing' is used to plot the position of known reference points at the ground (Schuckman, 2014). Here, all the images overlap with a very high percentage and contain the same reference points; the edges of the model box.

4.1.3 Output 2: Point cloud

A point cloud is a set of data within a defined coordinate system. If this coordinate system is defined with 3 dimensions, then each point will be given a coordinate similar to `(x,y,z,R,G,B)`. Because they most often represent the surface of an object, it can be used to extract the volume in addition to elevation changes in the surface. By subtracting the information in one point cloud from another, δz can be found. Here we use the file format ply, which is a polygon file format. The files are displayed using the open source program Meshlab.

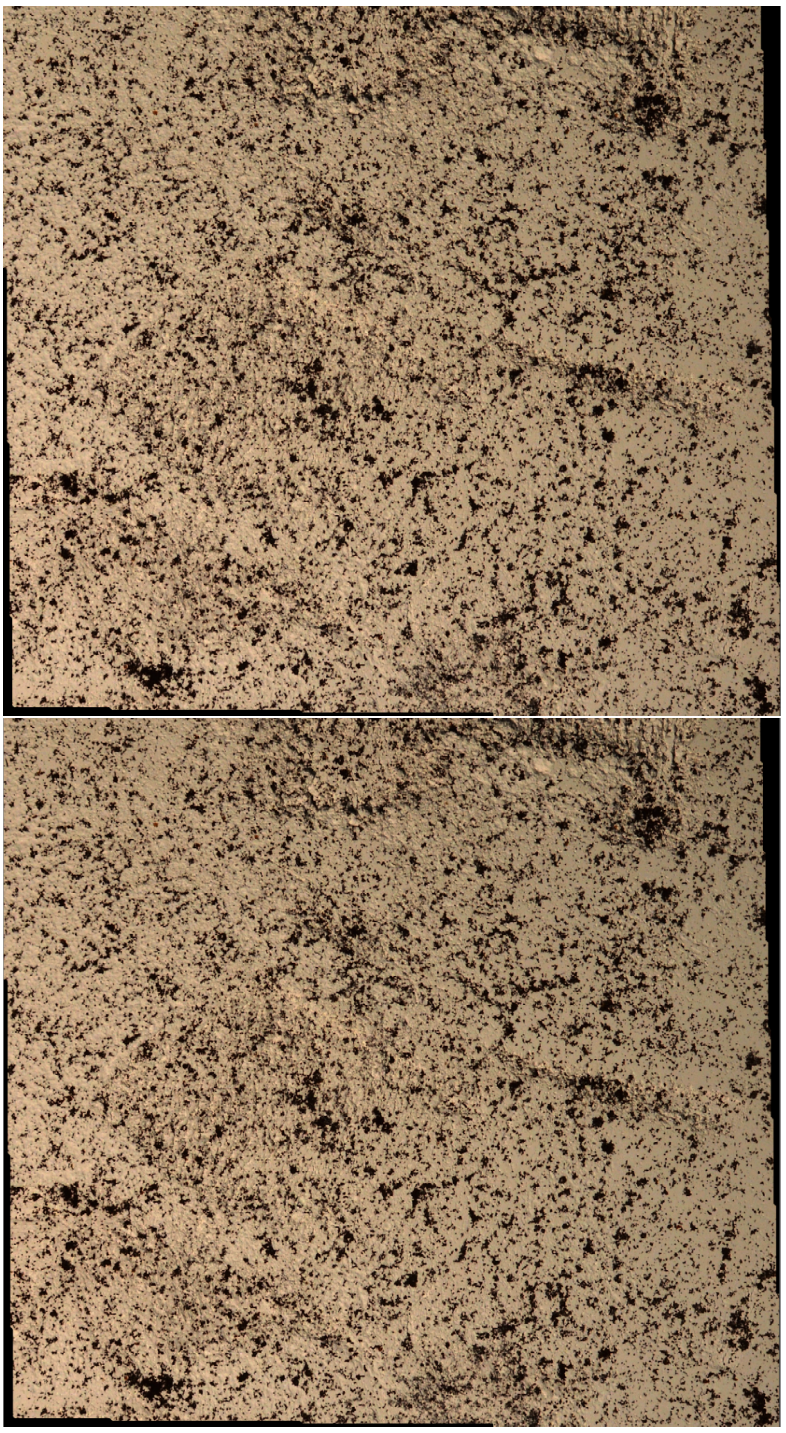

FIGURE 4.1: Orthophoto from first and last timestep before eruption in experiment 2. The images are free of distortion and can be used to acquire topographic changes at the surface. To see the difference between the two photos just by observing them aside is difficult, but the images contain high amount of information, giving them an average size of 15MB.

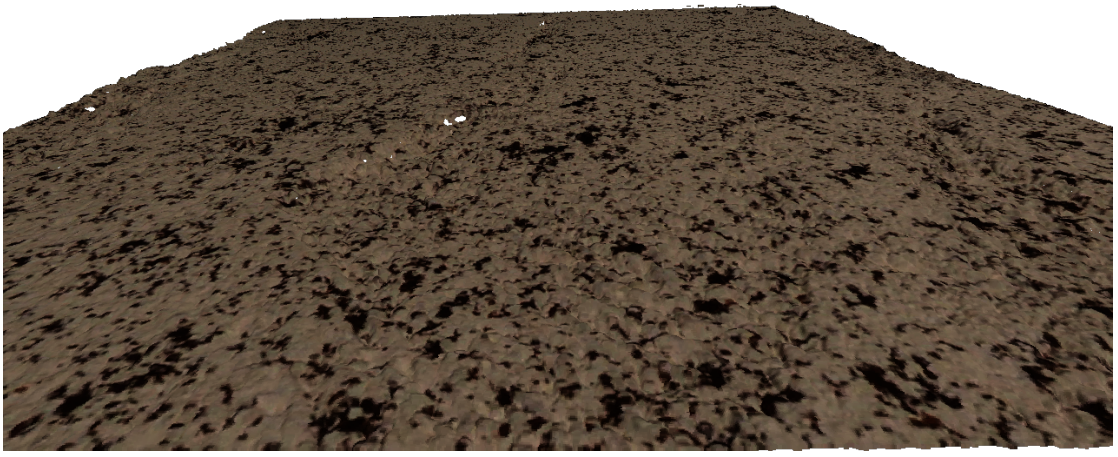

FIGURE 4.2: Point cloud file from time step 25 in exp.2 displayed in meshlab. The roughness of the surface becomes clear when zooming in, and the model can be used for looking closer at the deforming area.

4.1.4 Matlab workflow : Data analysis

The complete code and its functions can be found in Appendix C.

Start by importing the ortho photo and the point cloud file from the time step you want to start from (here; `T3`). The code `fmy` converts the ply file to a matrix with 6 rows `(x,y,z,R,G,B)` and as many columns as there are points. Separate the rows and transpose them.

The function `DigitalElevationModel` use the first ortho image and the coordinates of the point cloud to find z displacement (change in elevation); the output is called `DEM_orig`:

Before creating a loop that compares the ortho photos and point cloud files of the original image with the next time steps, we need to define the size of the templates and the exploration template used for comparison.
`Soft` defines the size of template in pixels, `p` is the fraction of overlap wanted between the templates and `delta` is the amount of pixels added to each side of the template to create the exploration area.

Then start the 'for' loop for the time steps of interest.

The loop starts by importing the ortho photo and the point cloud file, and prepares the point cloud matrix for the following digital elevation analysis, which gives the output of the displacement of x, y, z in mm. `x_p` and `y_p` defines the size of a pixel (in mm) in x and y direction.

The function `Firstpos` use the orthoimage from this time step, along with the size of the template and the overlap to compute the number of templates that will fit inside of the image. Then, to make sure that the matrixes with the deformation data are exactly the same size, we define them within the size of the template matrix `NT`.

For finding the displacement within each template, each templates need to be defined. In `tempdisp` are the positions `(x,y)` of the upper left pixel in each template defined, then this is used to define the template for the chosen `(i,j)`.

The template size is then used for confining an area within the `DEM` model of both time steps which contains the δz, and then used for defining the mean change in

elevation for this particular template. The area of comparison within the original image for this template is defined in the function `explorationarea`.

The function `Deforma` then use the definition of the template, the exploration area, the size of the template and delta to calculate the deformation in pixels in 2D. Then convert the deformation into mm, calculate the size of the original image in mm and calculate the coordinates of the template.

4.1.5 Deformation pattern from the surface analysis

The outputs from the matlab analysis are vector graphs in 2D and 3D with the same coordinate system that was created in MicMac 4.1.1. The scale is in mm, with the z-axis exaggerated 10 times to clearly display the deformation. The vectors describe (δx,δy,δz) from the first time step. To quantify the deformation, pcolor plots show the mm uplift.

The results from experiment 2 (see fig.4.3) show a deformation process with an uplift concentrated towards right up to 0.22mm, before ending up at 0.45mm two time steps before eruption. The horizontal displacement is directed outwards from the center of the deformation area, with a maximum value of -0.7mm in x-direction and 0.35mm in y-direction. The deformation starts in the right central part of the image, moving towards the upper left corner, right before the eruption. In this experiment, the horizontal deformation succeeds the vertical uplift by 0.25mm. Signal to noise ratio range from 1.83 to 4.5 in the elevation model.

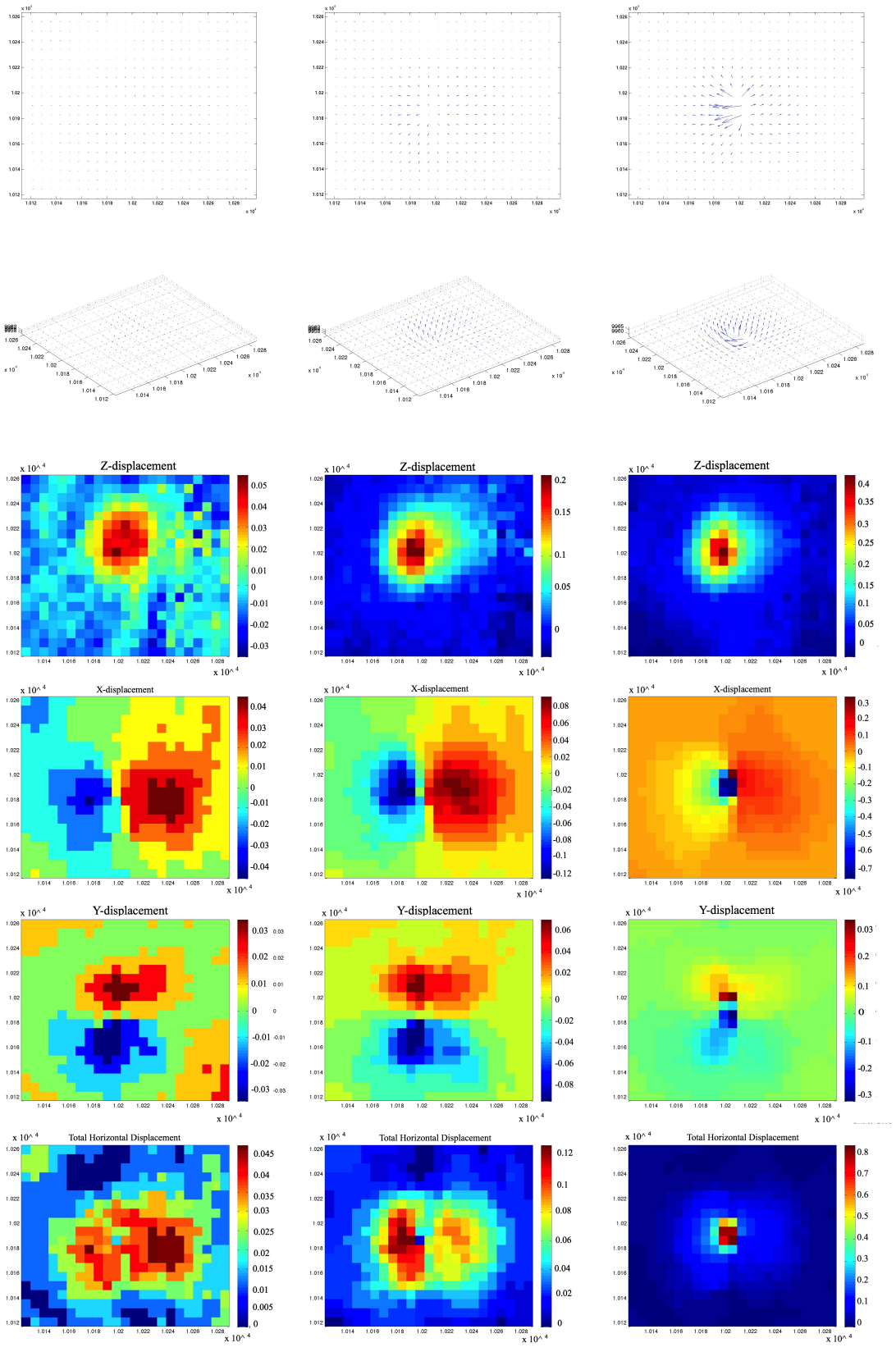

FIGURE 4.3: Results from photogrammetric analysis of E2. Top row: Quiver plot of horizontal displacement. 2nd row: 3D quiver plot of the total 3D displacement. 3rd row: Colorplot of z-displacement. 4th row: Colorplot of x-displacement. 5th row: Colorplot of y-displacement. 6th row: Colorplot of total horizontal displacement. Scale on axis is mm, where origo is located at $(10^4, 10^4, 10^4)$. In the vector 3D graph, the z-axis is exaggerated 10 times to increase the visibility of the deformation pattern.

4.2 Intrusion analysis

One of the objects of the analysis is to create a 3D model of the intrusion and to recreate the situation from the experiment in 3D, where the intrusion is located right beneath the surface deformation. In order to do this, the data from the photogrammetric method documenting the intrusion needs to be analyzed in order to produce a point cloud file. From the experimental part we know the orientation of the sheeted dikes relative to origo. All of the dikes from the experiments performed in this thesis had a north-south orientation when the y-axis is to the west and the x-axis is to the south.

4.2.1 Workflow for photogrammetric analysis

The workflow analysis for the intrusion is different from the workflow for the surface analysis in five ways:
1) There are no time steps, 2) During excavation, a level of the box were removed, 3) There are four more GCPs to consider, 4) We have two sets of data, one for each side of the intrusion. This might change depending on the shape of the intrusion, due to the number of photogrammetric analysis needed to document the complete shape. For the dikes in these experiments, the two-side analysis was sufficient. 5) The camera position is dynamic.

These changes imply that:
1) The workflow is much shorter since it only needs to compute one set of data (ortho photo and point cloud file).
2) The elevation of the surface of the model has changed with 5 cm, apply the changes for the existing GCPs in Dico-Appuis.xml.
3) The new GCPs must be defined in the Dico-Appuis file. Remember to consider the change in elevation (z = 8,5 cm to the top of the first layer).
4) The workflow must be created for both sets of data and they need to be processed within separate directories with customized workflow, Dico-Appuis.xml and Mesure-Appuis.xml.
5) Central images is needed for a convergent mode analysis. Define this in the Micmac-POV.xml file.

The redefined GCP in Dico-Appuis is 5 cm lower, due to removal of one level during excavation:

Corner 1: (10 000, 10 000, 9950)
Corner 2: (10 400, 10 000, 9950)
Corner 3: (10 400, 10 400, 9950)
Corner 4: (10 000, 10 400, 9950)

The new GCP defined in Dico-Appuis is defined at the level of the bottom of the box:

Corner 5: (10 400, 10 000, 9865)
Corner 6: (10 400, 10 400, 9865)
Corner 7: (10 000, 10 400, 9865)
Corner 8: (10 000, 10 000, 9865)

Remember to be consistent with the direction of the numbering. Here corner 5 and 6 has been defined at the side of corner 2 and 3, and corner 7 and 8 was defined at the side of corner 4 and 1.

For Mesure-Appuis, find all the new coordinates for the GCPs, but only choose the 4 GCPs pr. image that are highly visible in the photos. Since the photographic angle changes, then the GCPs used will change as well. Define GCPs in 5-7 images, half from the upper set of images and the rest from the lower angle. The upper images are used for confining the size of the box and to proper geo reference it, while the images from the near horizontal images are used for computing the shape of the intrusion. See example of this in Appendix B.

For the MICMAC Micmac-POV.xml, define the central image (NumC), which is the lower central image of the intrusion. Create a mask of the intrusion using this image (Example : `DSC_0015_Masq.tif` in image 4.4), and define its size in an xml file that goes in the same directory (Example : `DSC_0015_Masq.xml`). Examples of these files can be found in Appendix B. Then give the range of images used to compute the shape of the intrusion by defining NumMin and NumMax. These are repeated two times in this file.

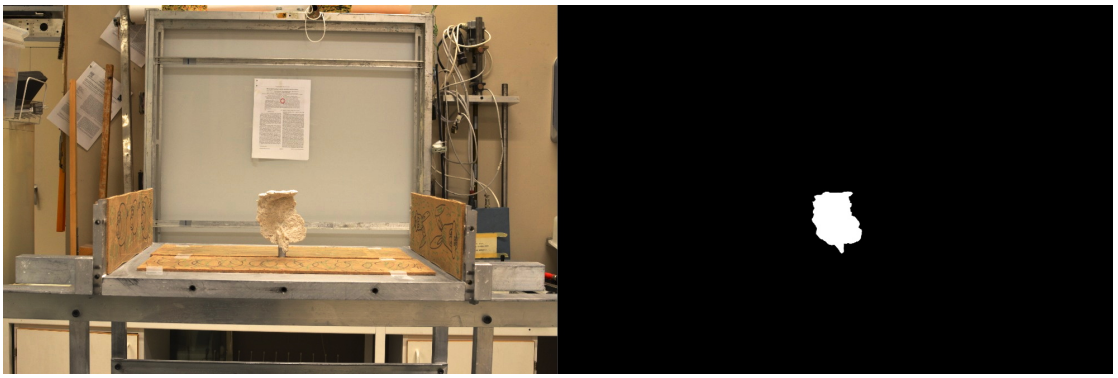

FIGURE 4.4: Masq of central image in Micmac-POV.xml

4.3 Results from photogrammetric analysis

The results from the photogrammetric analysis of the intrusion are a point cloud file that can be compiled using a program like Meshlab.

Both the point cloud file of the surface and the intrusion are geo referenced, so they can be compiled for a visual comparison. From figure 4.6b) you can see that the location of the bulge (Either represented by a raised surface or a hole in the surface. This is due to the photogrammetric analysis having trouble with reflective surfaces, such as for where the oil erupts.) is located right above the tip of the sheeted intrusions.

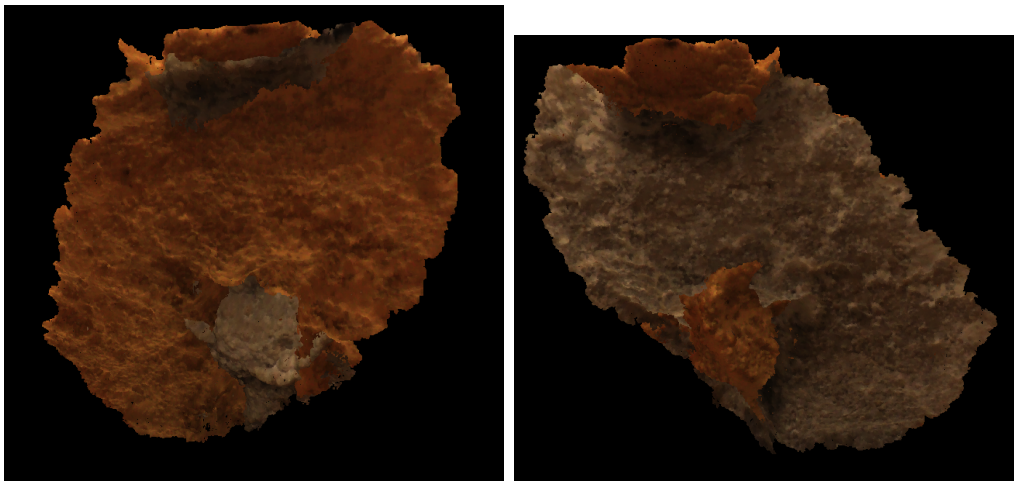

FIGURE 4.5: Point cloud of intrusion in exp. 2.

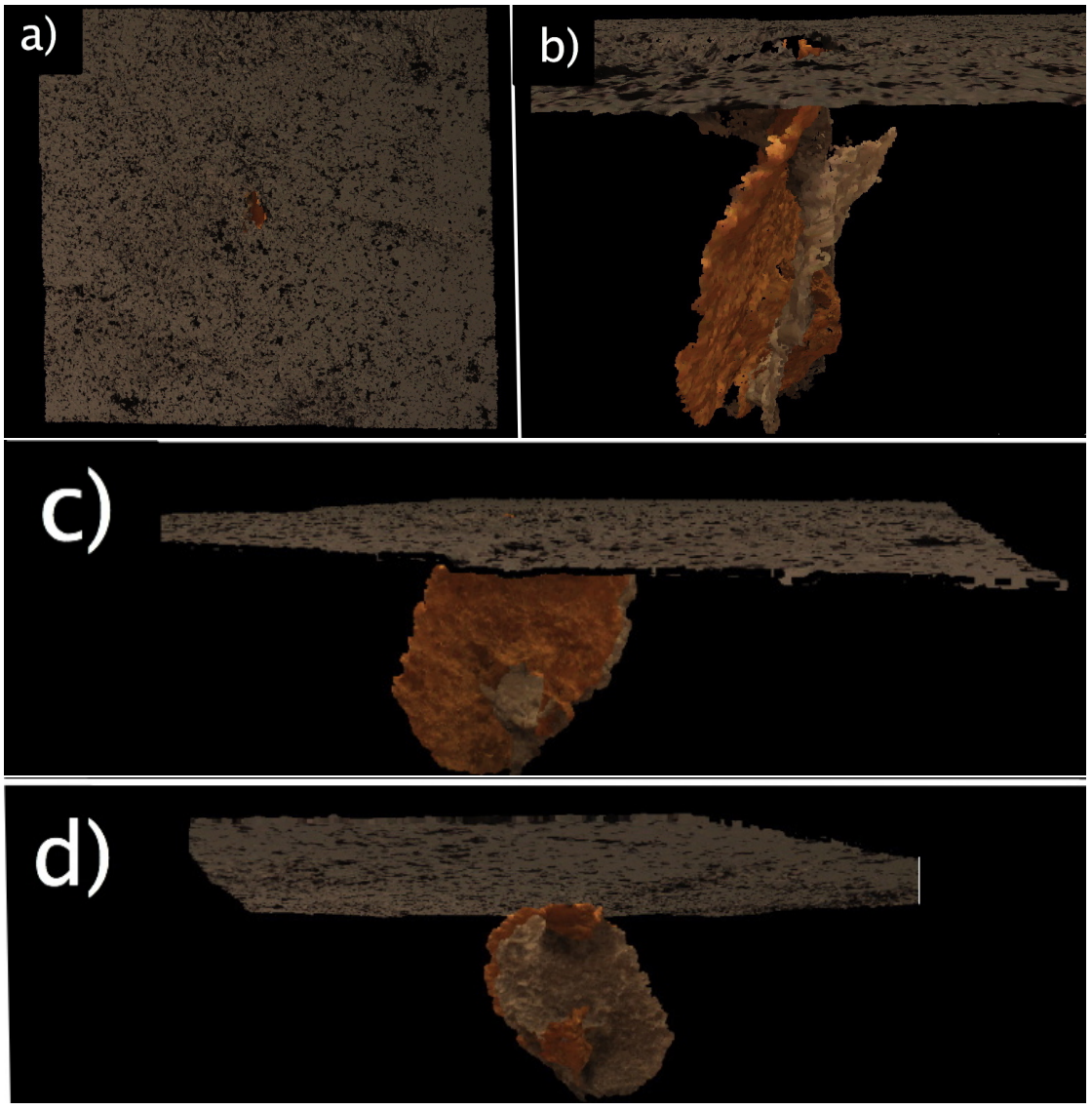

FIGURE 4.6: Point cloud of intrusion and surface from T25 in E2. **a.** Surface of the model. The intrusion is visible through the open fracture.**b.**From the side. **c.** From above **d.** From below.

Chapter 5

Results & Discussion

From the experimental part, a dataset of high temporal resolution was acquired using photogrammetry, covering the full time laps of the experiment. Each of the time steps represented by 4 overlapping photos taken simultaneously, was analyzed using photogrammetric analysis. This method included ortho rectification to compute an ortho image and creating a point cloud of the surface by defining a 3D coordinate system using the edges of the box as axis. Using the ortho photo, the 2D displacement (δx,δy) between each time step was detained. The point cloud was then compared to the ortho photo to acquire the change in surface elevation (δz). Since the surface of the model is flat, then there is no need for topographic corrections.

The intrusions, mostly sheeted dikes, were excavated and documented using a parted photogrammetric method where the amount of data is determined by the shape of the intrusion. The photogrammetric analysis gives a geo referenced point cloud file that compiles well with the point cloud file of the surface. The location of the bulge at the surface is located right above the intrusion, indicating that the geo referencing of the point cloud files are accurate. In addition, the two individual point cloud files of the intrusions compiled well, strengthening the latter assumption.

The main aim in this thesis is the developing og the method. To test the robustness of the method we therefor performed several experiments with the same parameters. They resulted in different deformation patterns and shapes of intrusions. By comparing the results of the experiments, we can find correlations between the deformation pattern and the shape of the intrusion.

5.1 Experimental results

5.1.1 Experiment: E2

The experiment lasted for about 1 min with 44 time steps. The measurable deformation started around T19, and erupted at T26. From the image analysis, the results from time step 19, 23 and 25 have therefore been chosen and displayed in figure 4.3. The intrusion was a sheeted dike with cone sheet features. Its texture was a bit fragile, most likely due to the oil had been heated and cooled during several experiments in the past, affecting the quality. It was replaced by new oil before next experiment. The surface of the model was poorly flattened affecting the local horizontality.

5.1.2 E3

The experiment lasted for 59 seconds, with 45 time steps. Camera 4 only worked for 39 of them, so time step 1-39 was analyzed. Measurable deformation started around time step T19, and the model erupted at T41. From the image analysis, time step 21, 29 and 39 have been chosen and displayed. The intrusion shape was a dike with cone sheet features. The texture was much better and the intrusion stronger than the two latter. This might be due to the change of oil.

The results from experiments 3 (see fig.5.1) shows a deformation process with a uplift concentrated towards right up to 0.45mm, before ending up at 0.96mm two time steps before eruption. The horizontal displacement is directed outwards from the center of the deforming area, with a maximum value of 0.4mm in x-direction and 0.25mm in y-direction. The deformation starts in the right central part of the image, increasing deformation occurs in the central part, right before the eruption. Signal to noise ratio is between 2.25 to 9.6 in the elevation model.

5.1.3 E5

The experiment lasted for 41 seconds, with 40 time steps. The measurable deformation starts at T11, and eruption occurs at T23. From the image analysis, time step 11, 18 and 21 has been chosen and displayed. The intrusion was a narrow

dike with cone sheet features. The experiment lasted shorter than the previous and the intrusion was smaller and more rounded.

The results from experiments 5 (see fig.5.2) show a deformation process with a uniform uplift up to 0.85mm, before peaking towards 2.5mm at the end of the experiment. The horizontal displacement is directed outwards from the center of deformation with a maximum value of -0.3mm in x-direction and -0.35mm in y direction right before the eruption. The deformation starts in the center of the image, concentrating towards the upper left corner, right before the eruption. Signal to noise ratio is between 2.125 to 8.5 in the elevation model.

5.1.4 E6

The experiment lasted for 30 seconds, with 23 time steps. The measurable deformation starts at T9 and eruption occurs at T20. From the image analysis, time step 9, 12 and 19 has been chosen and displayed. The shape of intrusion was a dike with a small cone sheet on the top. The bulge was clearly visible early on in the experiment, and this experiment lasted about half as long as the three others.

The results from experiments 6 (see fig.5.3) show a deformation process with a uniform uplift up to 0.4mm, before peaking towards 4,0mm at the end of the experiment. The horizontal displacement is directed outwards from the center of deformation, with a maximum value of -0.45mm in x-direction and 0.45mm in y-direction. The deformation starts in the upper right part of the image, moving towards the central part, right before the eruption. Signal to noise ratio range from 1.75 to 8 in the elevation model.

5.1.5 Figures: Deformation results

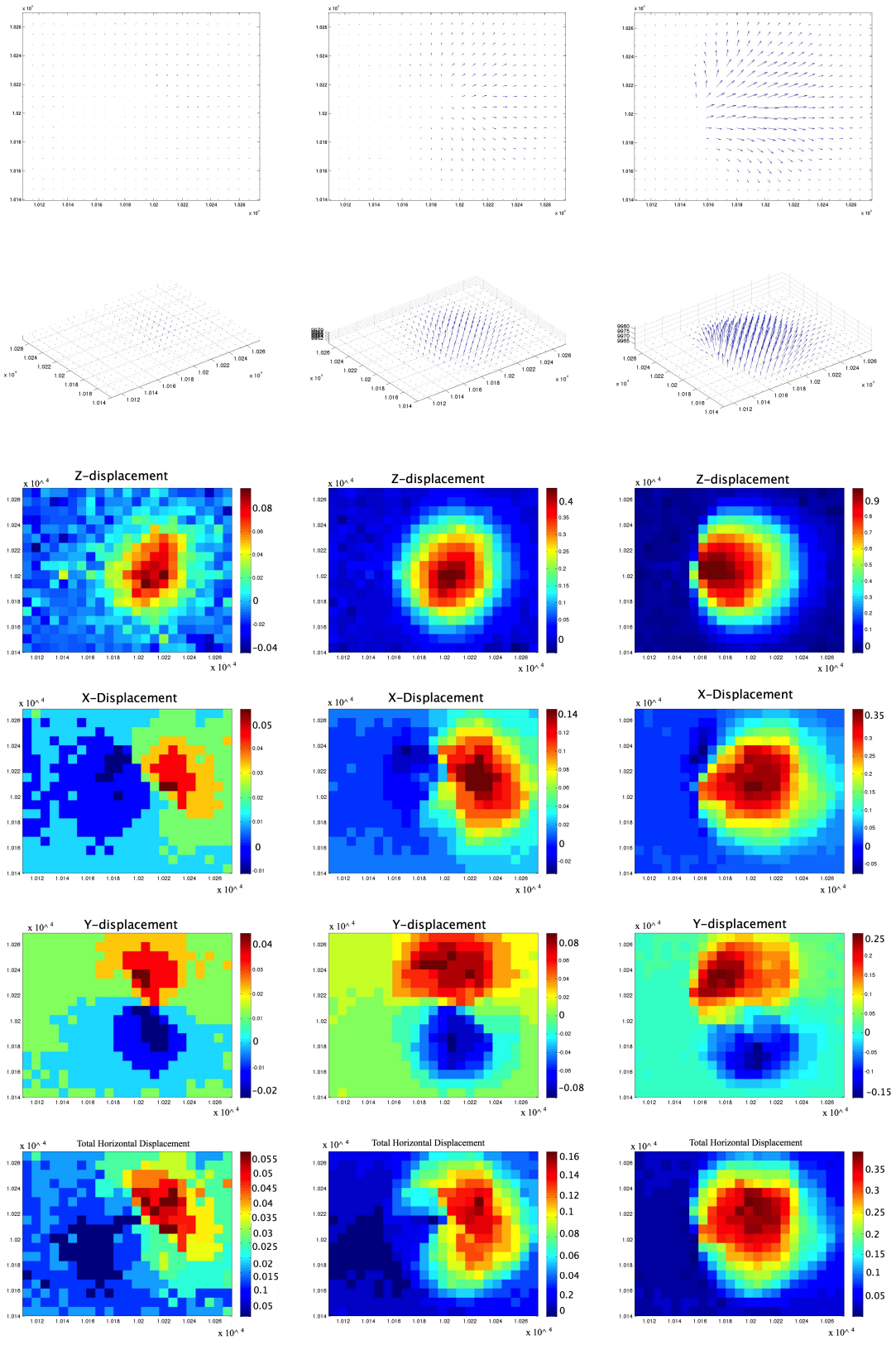

FIGURE 5.1: Results from photogrammetric analysis of E3. Top row: Quiver plot of horizontal displacement. 2nd row: 3D quiver plot of the total 3D displacement. 3rd row: Colorplot of z-displacement. 4th row: Colorplot of x-displacement. 5th row: Colorplot of y-displacement. 6th row: Colorplot of total horizontal displacement. Each column accounts for one timestep, increasing from left to right: T21, T29 and T39. Scale on axis is mm, where origo is located at $(10^4, 10^4, 10^4)$. In the vector 3D graph, the z-axis is exaggerated 10 times to increase the visibility of the deformation pattern.

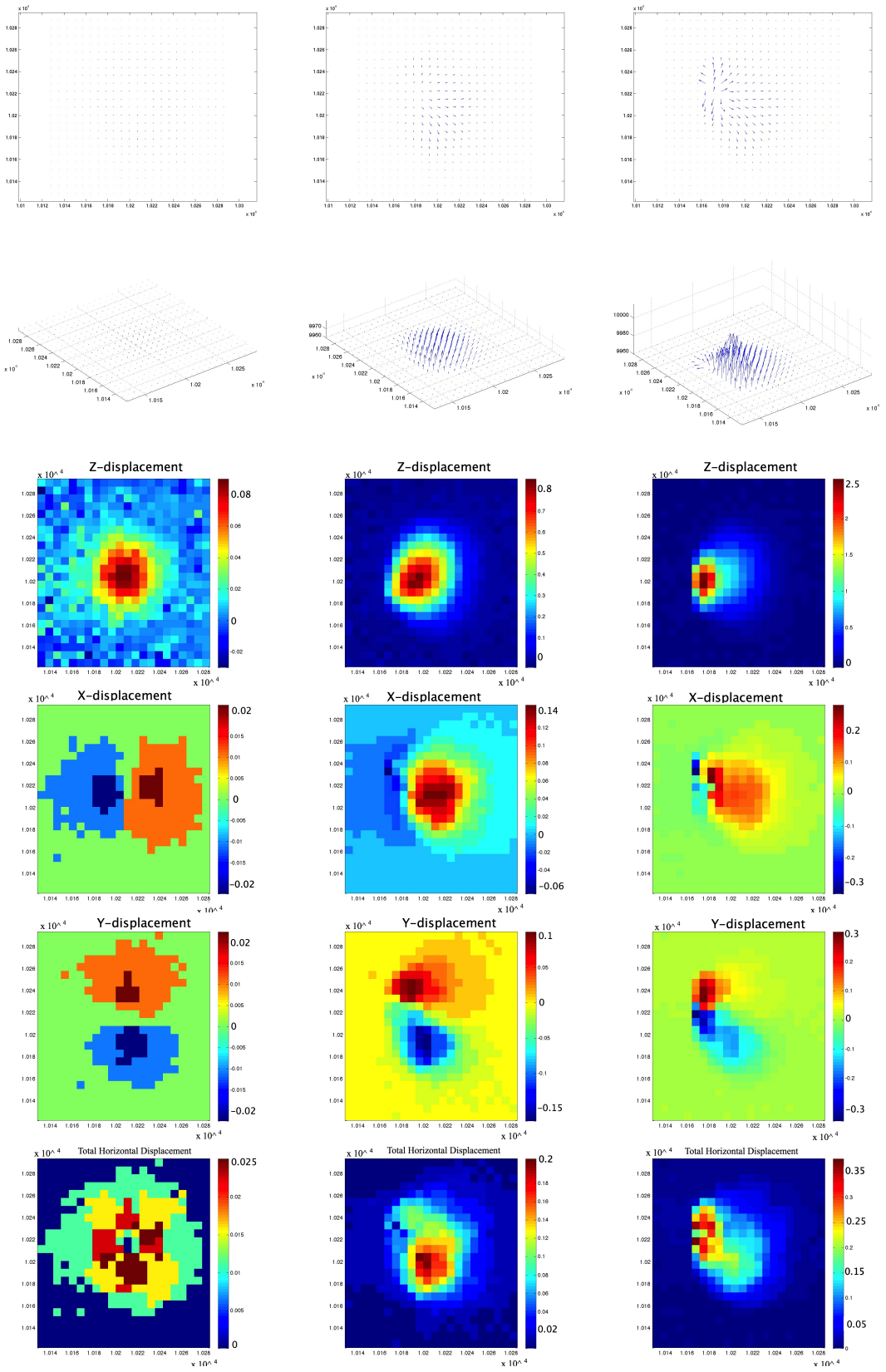

FIGURE 5.2: Results from photogrammetric analysis of E5. Same setup as in figure 5.1 with E3. Timesteps displayed here are T11, T18 and T21. Scale on axis is mm, where origo is located at $(10^4, 10^4, 10^4)$. In the vector 3D graph, the z-axis is exaggerated 10 times to increase the visibility of the deformation pattern.

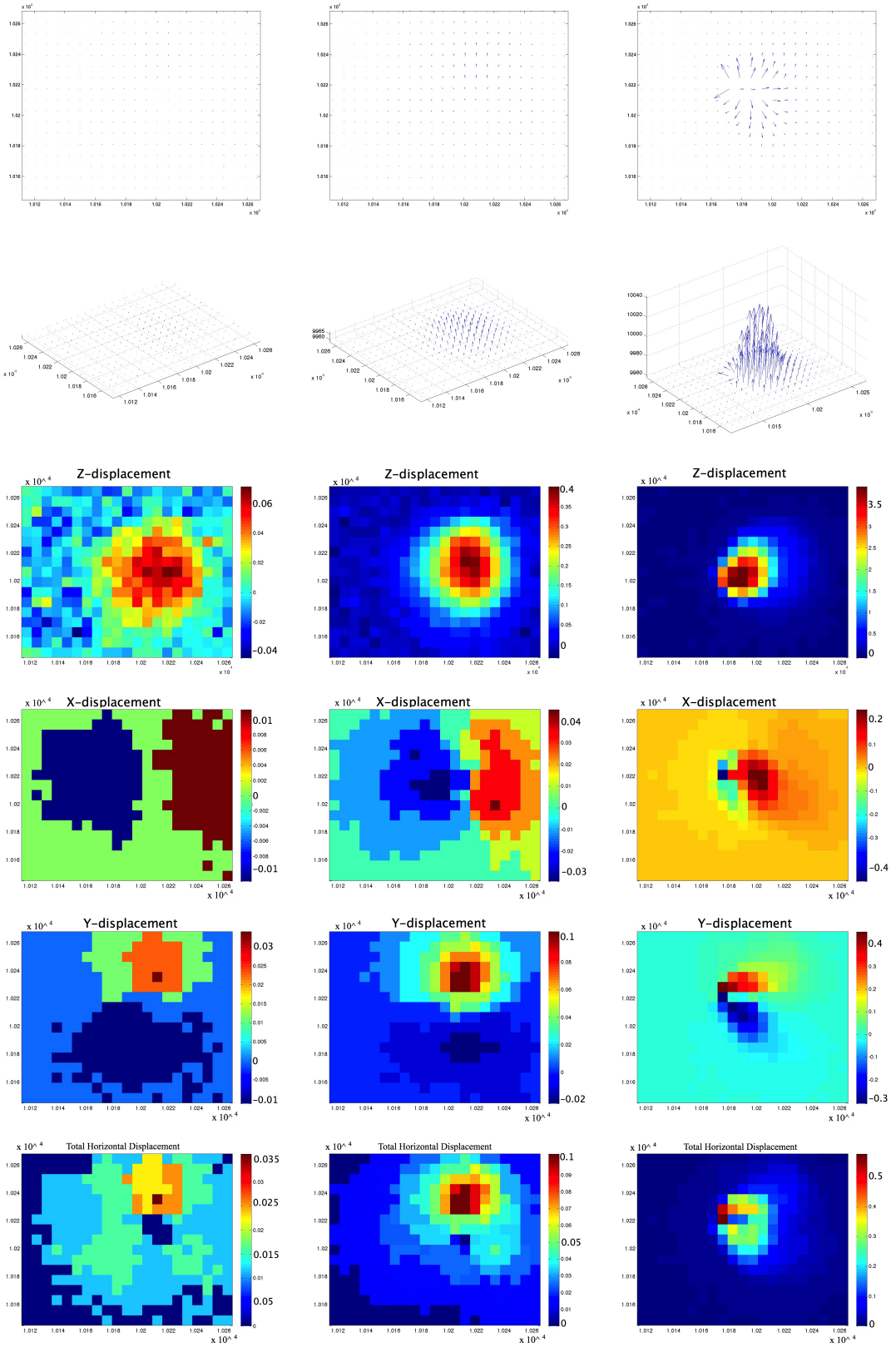

FIGURE 5.3: Results from photogrammetric analysis of E6. Same setup as in figure 5.1 with E3. Timesteps displayed here are T9, T12 and T19. Scale on axis is mm, where origo is located at $(10^4, 10^4, 10^4)$. In the vector 3D graph, the z-axis is exaggerated 10 times to increase the visibility of the deformation pattern.

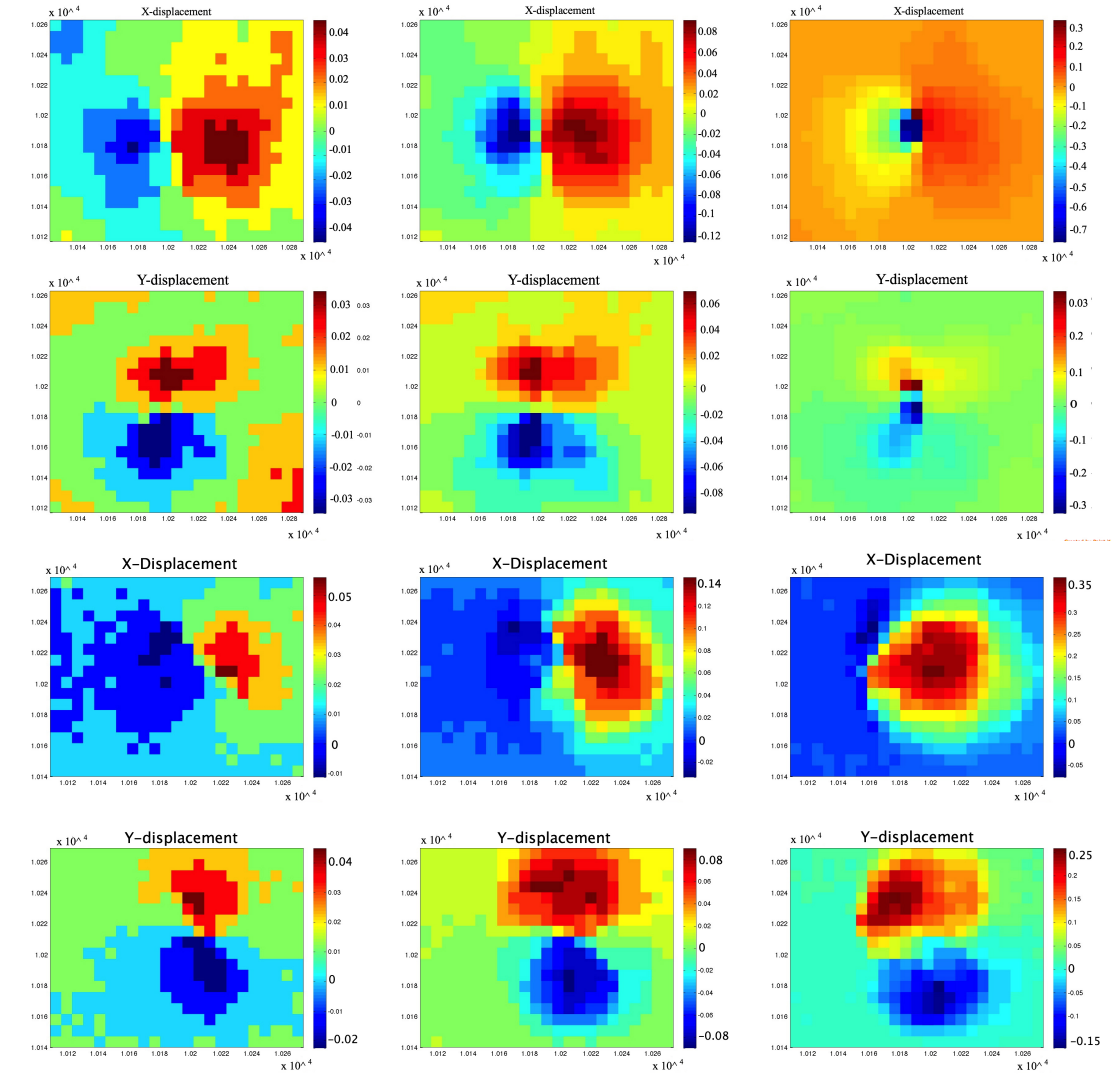

FIGURE 5.4: Comparing colorplots of the horizontal displacement and intrusion shapes from E2 and E3. From left to right: increasing deformation. Top:x-displacement from E2. Upper middle: y-displacement from E2. Middle: x-displacement from E3. Bottom: y-displacement from E3. Each column accounts for one timestep, increasing from left to right. Scale on axis is mm, where origo is located at $(10^4, 10^4, 10^4)$. The images display the different intrusions; a = E2, b = E3.

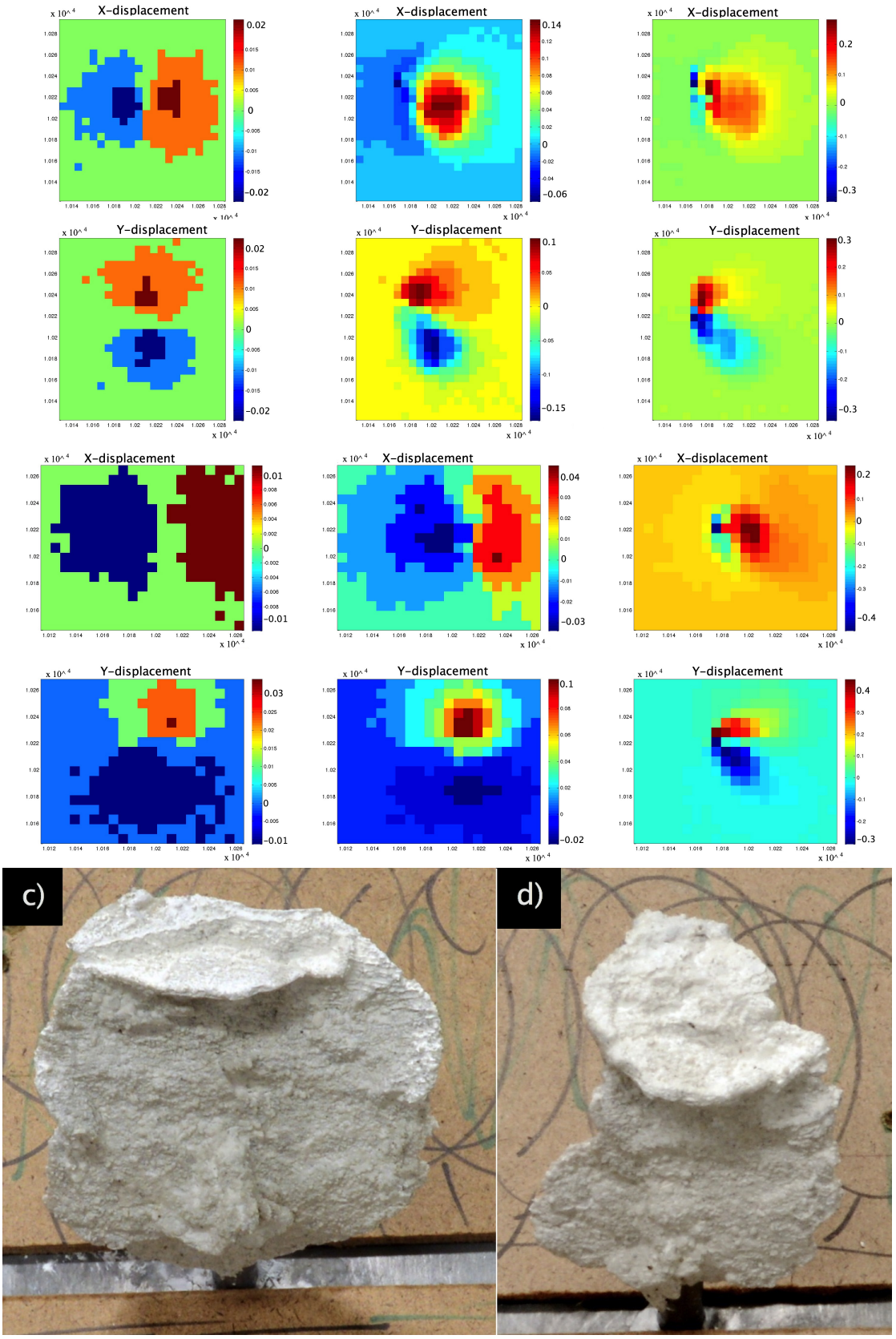

FIGURE 5.5: Comparing colorplots of the horizontal displacement and intrusion shapes from E5 and E6. From left to right: increasing deformation. Top: x-displacement from E5. Upper middle: y-displacement from E5. Middle: x-displacement from E6. Bottom: y-displacement from E6. Each column accounts for one timestep, increasing from left to right Scale on axis is mm, where origo is located at $(10^4, 10^4, 10^4)$. The images display the different intrusions; c = E5, d = E6.

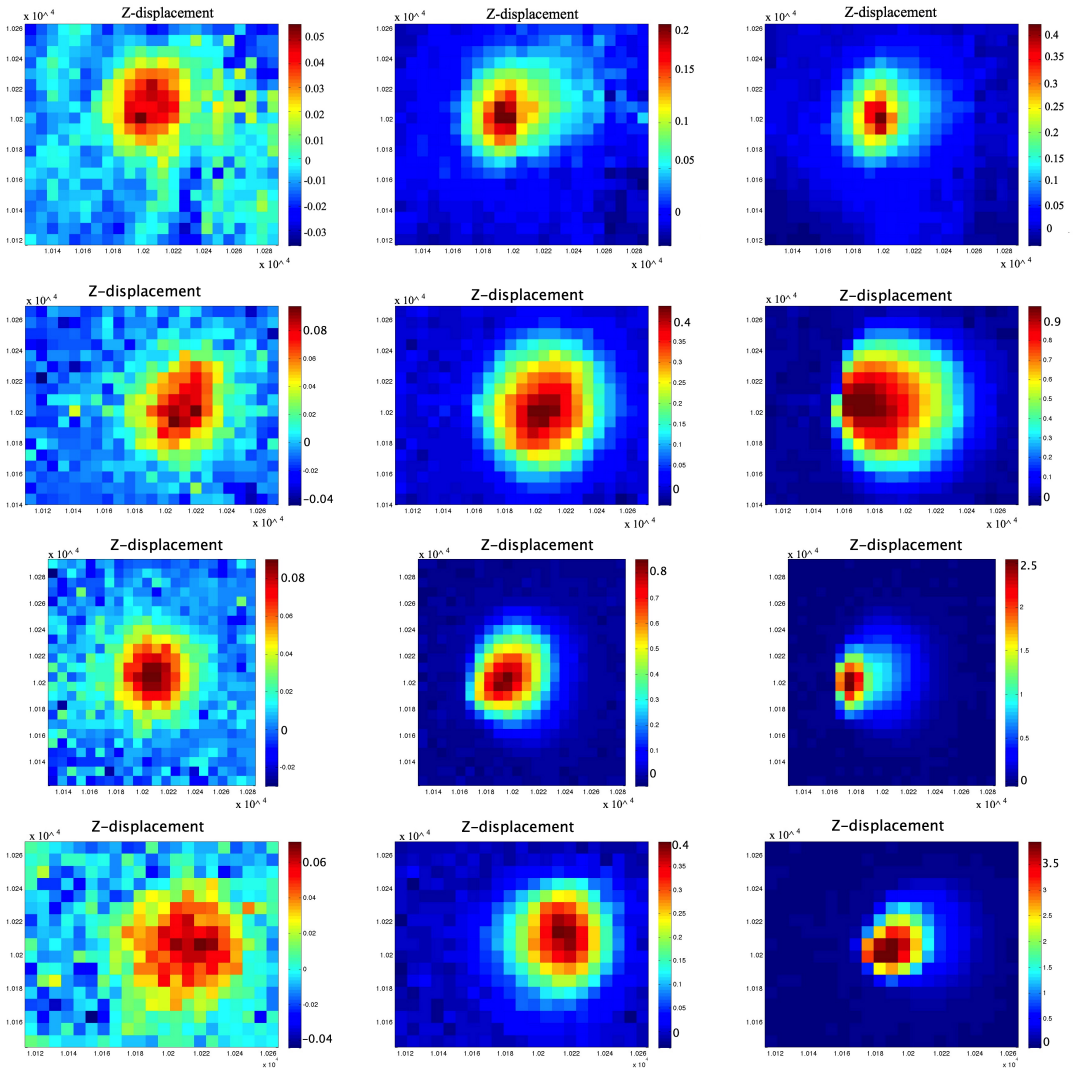

FIGURE 5.6: Comparing colorplots of the elevation displacement. From left to right: increasing deformation. Top: z-displacement from E2. Upper middle: z-displacement from E3. Middle: z-displacement from E5. Bottom: z-displacement from E6. Each column accounts for one timestep, increasing from left to right. Scale on axis is mm, where origo is located at $(10^4, 10^4, 10^4)$.

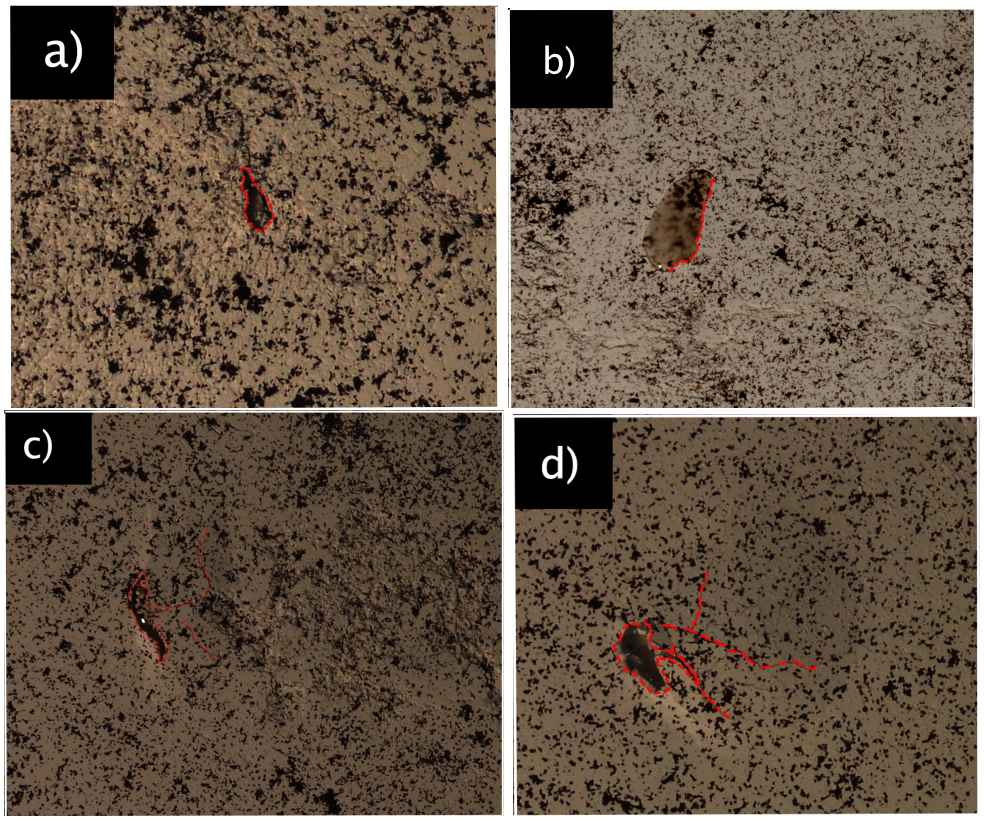

FIGURE 5.7: Comparison of ortho images taken directly after the eruption of the oil, from photogrammetric analysis of E2, E3, E5 and E6. The photos are cropped versions of the ortho photos. The red dotted lines define the area of fracturing. **a.** Ortho image from T25 in E2. The fracture is wide, with only a fraction of the oil is visible. **b.** Image from camera 1 in T41, E3. The fracture is long and narrow, with a lot of oil erupted. **c.** Orthoimage from T23 in E5. The fracture is wide and located at the edge of the visible bulge. The oil is visible within the opening, and you can se fracture network continuing to the left. **d.** Ortho image from T20 in E6. The fracture is wide and located at the edge of the visible bulge, but there is little oil. Joints can be followed from the fracture and over the bulge.

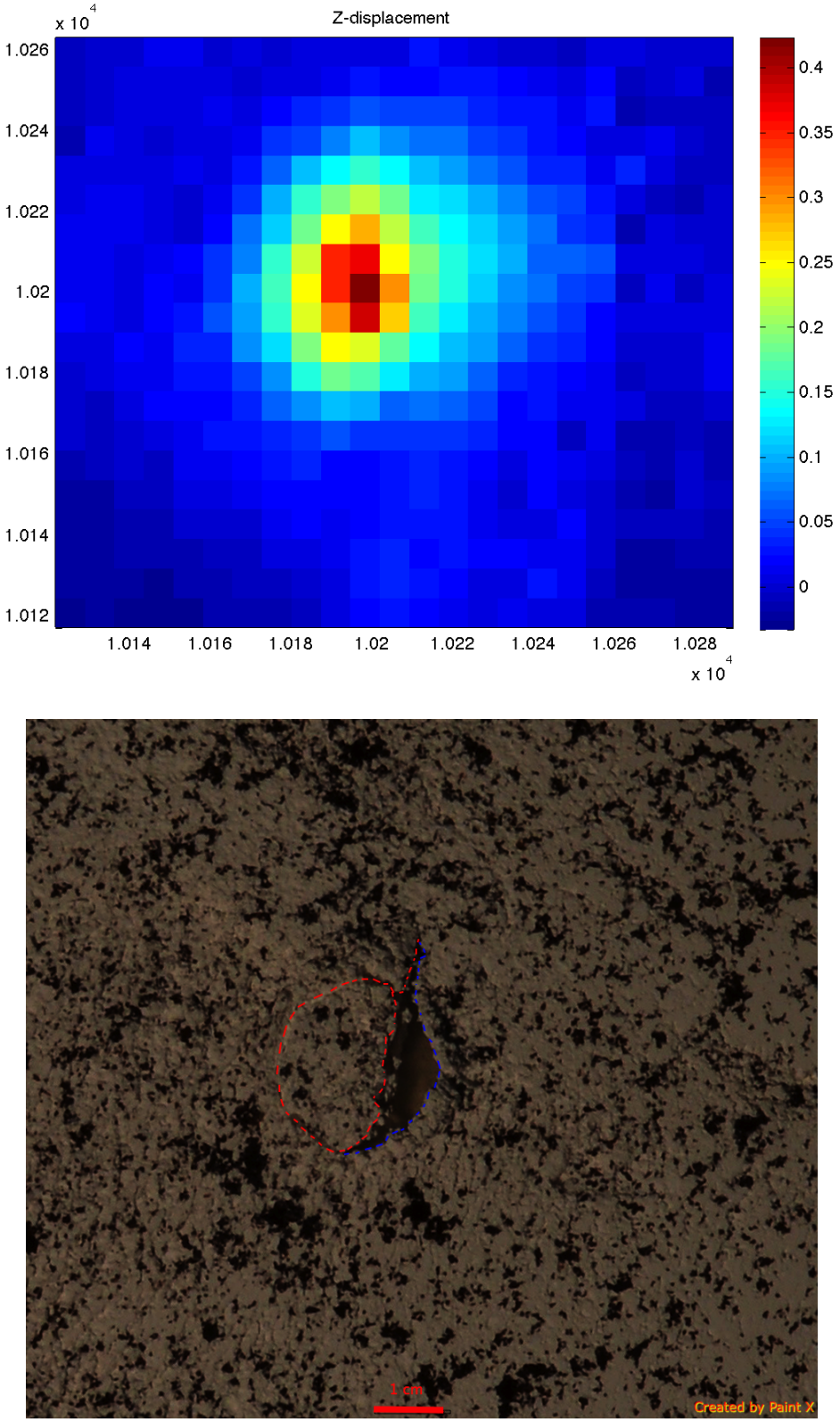

FIGURE 5.8: Comparison of z-displacement and ortho image from photogrammetric analysis of exp. 2. Scale on the plot (from time step 25) axis is mm, where origo is located at $(10^4, 10^4, 10^4)$. The photo is a cropped version of the ortho photo from time step 31 in experiment no.2. The red dotted lines define the area of uplift, and the blue dotted lines define the area where the oil erupted.

5.1.6 Comparing results from the photogrammetric analysis

We start by looking at the example from E2 presented in chapter 4.1.5, figure 4.3. It display the deformation pattern from T19 were the deformation became visible, T23 where the deformation started to accelerate, and T25, right before the eruption occurred. The horizontal deformation pattern (x-displacement in row 4, y-displacement in row 5, Displacement in row 6) is clearly symmetrical and the displacement outwards from both sides of the deformation center indicates uplift. The evolving displacement can be followed from early time steps in the experiment, giving away the position of what is assumed to be the propagating tip of the dike. Right before the eruption, in time step 25, the patterns display a sharp contrast of two templates (points) moving opposite ways, within the central outwards displacement. This is assumed to be due to the forming of a fracture, which is displayed in fig.5.8. It could also be due to noise, but the maximum noise in the horizontal displacement is 0.05, and the signals here are between 0.3-0.7mm. From the ortho photos one can barely see a narrow rift in time step 27, two-time steps after the pattern appeared in the analysis, and the deformation becomes clearly visual first in time step 31.

By comparing the horizontal displacement of the four experiments in figure 5.4 and 5.5, we can find patterns that can indicate which type of intrusion we have. Since all the intrusions are sheeted dikes, then the deformation patterns will be generally similar.

Comparing experiment 2 and 3, you can see two different regimes. E2 is fairly symmetrical, having an evenly distributed displacement in all directions. E3 is symmetrical in y-direction, but in x-direction all the displacements is directed towards the right. Being sheeted intrusions that propagate by fracturing the flour, one of the horizontal displacements indicates the thickness of the intrusion, while the other would indicate the width or the shape of the propagating tip. Since the y-displacements were similar, and since we now know the orientation of the intrusion relative to origo, I would say that the thickness of the intrusion could be indicated by the y-displacements. The intrusions were about the same thickness, as is the y-displacements. The values in the x-displacements are similar too, but since the distribution patterns are completely different then they indicate two different shapes. The evenly distributed pattern from E2 suits well with the straight shape

of the intrusion in figure a. 5.4, where I assume that the intrusion has propagated straight up from the inlet without bending. The pattern from E3 is broader and more defined, indicating that it is affected by an intrusion with a more horizontal shape. The resulting shape of intrusion 3 (b. in fig 5.4) fits well to this description with its sheeted dike with a flat top that is bent towards the horizontal when it approaches the surface of the model.

We then compare the results from the horizontal displacement from E5 and E6, displayed in figure 5.5. Both of the x-displacements are more asymmetrical than E2, looking more like E3 in the displacement distribution. At the step right before the eruption, both have a sharp contrasting displacement, where the flour is being pushed away from the center in both directions. This is unlike E3, which had more of a one-way displacement. In E2, I interpreted the contrast as an upcoming rift. The y-displacement, which I interpreted as the thickness of the sheet, is changing during the experiment in E6. From T12, when the deformation starts to concentrate around a small area, you can see that the movement is asymmetrical, moving distinctively north. Then right before the eruption, it turns symmetrical with a sharp contrast in the middle. In E5, the displacement in y-direction is more symmetrical than E6 from the start to the end, but slightly less than E2 and E3. Comparing the intrusions, E5 is very similar to E2, except for the two horizontal features is located below the surface, while it in E2 was in the top layer. E6 has a rounded cone sheet shaped feature on top of the sheeted dike, which could be responsible for the final symmetrical displacement pattern.

In figure 5.6 we compare the elevation displacement for all the four experiments. The time steps are from the figures 4.3, 5.1, 5.2 and 5.3. In the first time step, the signal vs. noise ratio is visual. The deformation has just started, but we can se points of displacements over the whole surface. The signal to noise ratio range from 1.75 to 9.6 in the four experiments, giving that the weakest signal still is 175 % stronger than the highest value of the noise. In the second time step, the uplift in all experiments is clearly visual and separated from the surroundings. In this step, E3 and E6 are fairly similar with the same shape and value of the uplift. E2 is a bit elongated with a concentrated uplift to the left. E5 is more concentrated with the highest uplift of all the experiments. Then, in the last time step, right before the eruption, E2 and E5 concentrate about a narrow point. While E2 has a graded uplift, E5 has a sharp transition from high to low z-displacement indicating a zone of greater stress rate. This sharp transition with high stress rate is also

found to the left in E3. E6 has the highest uplift, and it is shaped like a circle with a relatively sharp transition to zero uplift. The ortho image taken after each eruption is displayed in figure 5.7 above. In this image you can see that E3 has an elongated, narrow fracture with lots of oil pumped out. This fits with the description of its vertical uplift being broad and having a strong gradient to the left. E5 has an elongated uplift with a wide fracture on the left side. This fits with the strong gradient and uplift, creating an area of high stress. E6 has a large, rounded bulge with a wide fracture on the left rim, which explains the circular uplift mentioned above.

5.1.7 Errors

Figure 5.9 displays some of the errors occurring during the analysis of experiment 2. The upper image displays the point cloud file from the last time step after the eruption of the oil. The oil is a transparent fluid, creating trouble for Tapioca to find any feature points, and therefor this section appears blank. This affects the next step, the matlab analysis, as seen in the central figure. Due to complete transformation of the area where the oil erupted, both because of fractioning of the flour where the oil erupts and to the oil covering parts of the surface, the defined templates in this area are unable to correlate to the original image. This effect has also been mentioned by Donnadieu et al. (2003). The analysis then assumes that they have been moved outside of its exploration area and displays them with the largest vectors. This is confirmed by looking at the surrounding templates (each represented by a vector) which are normal sized, making it difficult to believe that such a large translation could happen without affecting the areas next to it. These large anomalies can also be seen in the lower figure, where the z-displacement went from 0.8mm to 2.5mm in one time step.

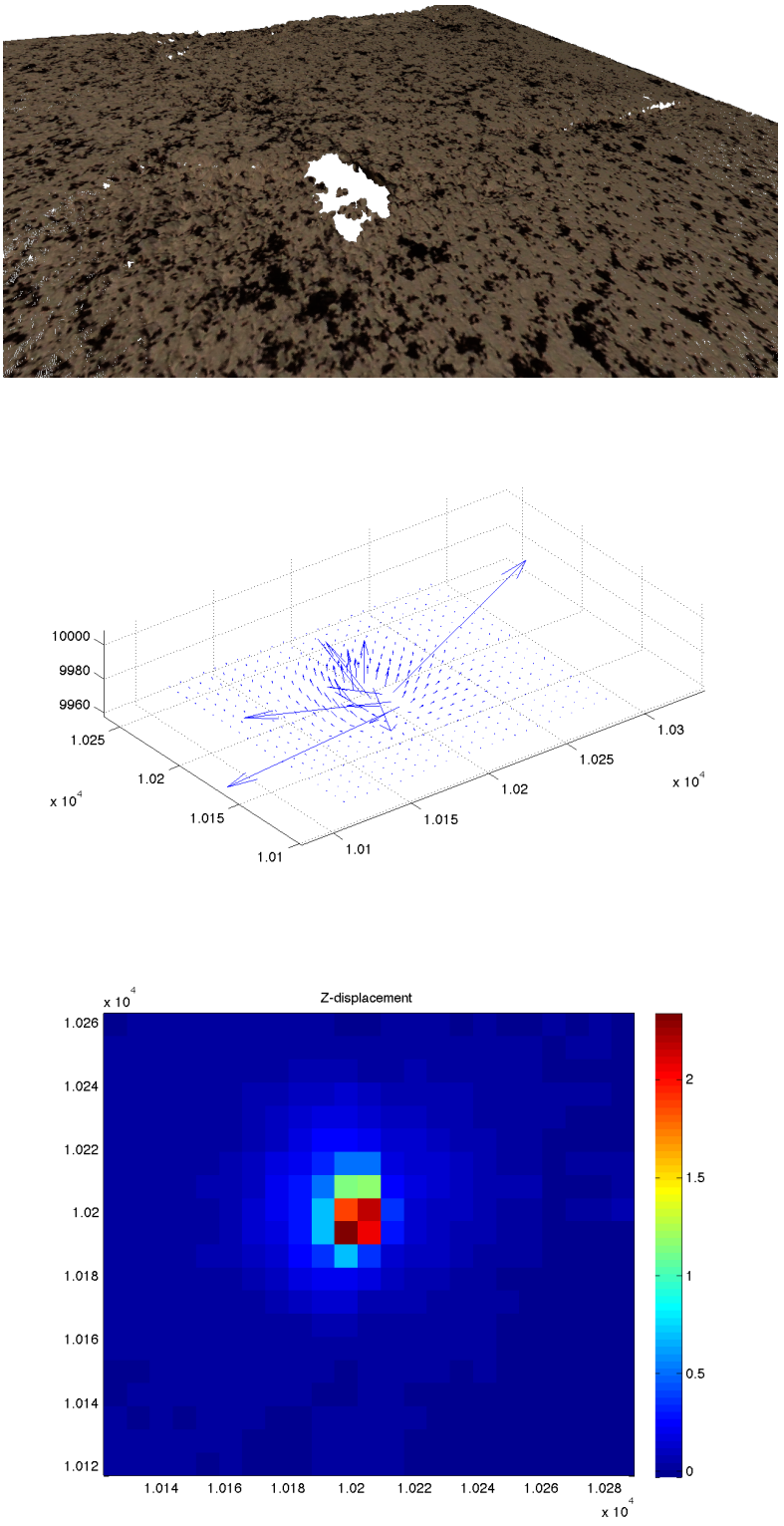

FIGURE 5.9: Errors in photogrammetric analysis. Top: Point cloud file of time step 27 in exp.2. The empty space is where the area has been altered by fractioning and adding of material from within the model, making it unrecognizable for correlation. Centre: Vector graph from the same time step, where each vector represents a template. The large vectors represent the altered area. Bottom: Z-displacement of the same time step, giving a positive value of 2.5mm change in height. Compared to the last time step before eruption (0.8mm), the value increased by 1.7mm in two time steps.

5.2 Comparing with former work

The laboratory experiment provides a method for monitoring the model from a vertical point of view with multiple cameras (with a focal length equivalent to 35mm) while the experiment is running. This aero triangulation photogrammetry method is similar to the stereoscopic photogrammetry method presented by Donnadieu et al. (2003), but use four images pr. time step instead of two, giving a higher resolution (0.15mm to 0.114mm). In Donnadieu et al. (2003), the grids are overlain the model manually, while we apply this in the matlab analysis, in this way avoiding any physical and optical effects the application of the grids might have on the flour. This photogrammetric method is more accurate comparing to other methods such as Microsoft Kinect by Tortini et al. (2013) and the laser method presented by Lague et al. (2003).. The image resolution using Kinect is lower (`640x480 vs 6016x4000` pixels) and the vertical resolutions of both methods are 1mm compared to 0.114mm in this experimental method. In addition, the two methods do not separate the uplift from the horizontal displacement, giving less information about the total deformation process. The Kinect have a higher frequency rate of acquisition (30 acquisitions pr sek vs 2 acquisitions pr sek), but the quality of the data is lower, decreasing the signal to noise ratio and accumulating larger quantities of noise over time. The signal to noise ratio for the results from this photogrammetry analysis is averaged to 5.3, ranging between 1.75 and 9. This accounts for a signal noise between 0.01-0.05mm when the values from the analysis of the z-displacement range from 0.055-0.45mm. Another method of continuous measurements using videogrammetry is N-View (Cecchi et al., 2003). To compute the 3D displacement, it needs images from multiple views at the same time, complicating the acquisition process. To compare, we only need four cameras in a fixed position to acquire the same high resolution of the model. The four cameras can easily be switched with four video cameras to match the continuous monitoring of N-View. The moiré projector method presented by Galland (2012) is a monoscopic view method Donnadieu et al. (2003) using a video camera that captures the deformation. This is done by applying a fringe pattern on the surface of the model, created by a projector placed vertically above it. This method gives the 3D surface deformation, but cannot distinguish between the horizontal and the vertical displacement. As mentioned by Galland (2012), this analogue model does not take in to account for the complexity of the natural volcanoes, such as

layering creating heterogeneity in the mechanical behavior of the rock, topography created by previous volcanic activity or regional tectonic deformation. Cecchi et al. (2003); Donnadieu et al. (2003); Tortini et al. (2013) all had analogue models with topography, which is a natural step further for developing this method towards a more realistic model with data that can be compared with real geodetic data.

Chapter 6

Conclusion and future prospects

We have developed a quantitative method for monitoring and modeling the dynamic surface that is the results of experimental modeling of a realistic sheeted intrusion in a 3D setup. The method gives sub pixel resolution at 0.114mm and allows for the horizontal and vertical displacement to be quantified separately. It is then a more realistic dataset that can be compared to real geodetic models, to quantitatively test their validity.

By using vegetable oil, which solidifies at room temperature, the intrusion can be excavated. By keeping a constant pressure in the inlet tube, the shape of the intrusion are most likely kept constant by the help of the cohesive host material. The 3D shape of the dynamic surface of the model is acquired through the fixed angle photogrammetry method, and the dataset to compute the 3D shape of the intrusion is acquired through the dynamic angle photogrammetry method. By geo referencing both 3D models, we can se that the location of the intrusion is right beneath the area of deformation at the surface.

From the fixed photogrammetry method analysis we get a dataset, which gives us, an ortho photo and 3D point cloud of the flour surface.
The ortho photo gives us displacement in 2D (δx,δy), and the point cloud gives us the vertical displacement (δz). By analyzing each time step of the experiment, we get a dataset of the 3D displacement over time.

Suggestions for further work would be to test the data against real geodetic models, for comparing the deformation patterns that are linked to the different shapes and sizes of the magmatic intrusions. Adding topography and layering to the analogue

model could improve the data. This would add the necessary complexity to the simple model for a more realistic result. This will of course need to be tested for different volcanic regimes, without going into detail about how this should be done.

Appendix A

Excel sheet for calculating flour density

Time (s)	**Mass (kg)**	**Height of walls**	**Thickness**	**Mes1**	**Mes2**	**Mes3**	**Mes4**
Rikke 01	Experiment date: 1-3 april						
	=(0,4*0,4*(0,034+0,06)-P6)*1050						
1	=(0,4*0,4*(0,034+0,06)-P7)*1050	0,1856	0,01	0,05845	0,065	0,0683	0,0609
180	=(0,4*0,4*(0,034+0,06)-P8)*1050	0,1856	0,01	0,0784	0,084	0,0765	0,0758
270	=(0,4*0,4*(0,034+0,06)-P9)*1050	0,1856	0,01	0,081	0,0805	0,0835	0,0785
270	=(0,4*0,4*(0,034+0,06)-P10)*1050	0,1856	0,01	0,0859	0,083	0,0833	0,0844

Thickness1	**Thickness2**	**Thickness3**	**Thickness4**	**Ave Thickness**	**Depth pipe**	**Volume cube**	**Volume inlet**
							=PI()*0,005*0,005*0,034
=C7-D7-E7	=C7-D7-F7	=C7-D7-G7	=C7-D7-H7	=(I7+J7+K7+L7)/4	=M7-0,034	=M7*0,4*0,4	=PI()*0,005*0,005*0,034
=C8-D8-E8	=C8-D8-F8	=C8-D8-G8	=C8-D8-H8	=(I8+J8+K8+L8)/4	=M8-0,034	=M8*0,4*0,4	=PI()*0,005*0,005*0,034
=C9-D9-E9	=C9-D9-F9	=C9-D9-G9	=C9-D9-H9	=(I9+J9+K9+L9)/4	=M9-0,034	=M9*0,4*0,4	=PI()*0,005*0,005*0,034
=C10-D10-E10	=C10-D10-F10	=C10-D10-G10	=C10-D10-H10	=(I10+J10+K10+L10)/4	=M10-0,034	=M10*0,4*0,4	=PI()*0,005*0,005*0,034

Volume frame	**Volume silice**	**Densite (kg/m3)**		**Density**
0	=O7-P7-Q7			=B7/R7
0	=O8-P8-Q8			=B8/R8
0	=O9-P9-Q9			=B9/R9
0	=O10-P10-Q10			=B10/R10

Appendix B

Workflow for Photogrammetric analysis of surface, part 1

In this appendix are the workflows and xml files for the full photogrammetric analysis in MicMac:

B1)	Main workflow for surface analysis in MicMac
B2)	Dico-appuis for surface analysis
B3)	Mesure-appuis for surface analysis

- **Surface Analysis: Main Workflow –**

```
export PATH=/Applications/MicMac/bin:$PATH

cd T1
Tapioca All .*.JPG -1
Tapas Fraser .*.JPG Out=Ground
GCPBascule .*.JPG Ground Terrain-Ground Dico-Appuis.xml
Mesure-Appuis.xml
Tarama .*.JPG Terrain-Ground
SaisieMasq TA/TA_LeChantier.tif
Malt Ortho .*.JPG Terrain-Ground ZoomF=1
Tawny Ortho-MEC-Malt/
Nuage2Ply MEC-Malt/NuageImProf_STD-MALT_Etape_9.xml
Attr=Ortho-MEC-Malt/Ortho_Redr.tif
MICMAC Micmac-ortho-cloud.xml
cd ..

for (( i = 3 ; i<=27 ; i++ ))
do
cd T$i

cp -R ../T1/Ori-Terrain-Ground Ori-Terrain-Ground
cp -R ../T1/TA TA

Malt Ortho .*.JPG Terrain-Ground ZoomF=1
Tawny Ortho-MEC-Malt/
Nuage2Ply MEC-Malt/NuageImProf_STD-MALT_Etape_9.xml
Attr=Ortho-MEC-Malt/Ortho-Eg-Test-Redr.tif

cd ..
done
```

-

- **Surface Analysis: Dico-Appuis –**

```
<?xml version="1.0" ?>
<Global>
     <DicoAppuisFlottant>
          <OneAppuisDAF>
               <Pt>10000 10000 10000</Pt>
               <NamePt>1</NamePt>
               <Incertitude>3 3
2</Incertitude>
          </OneAppuisDAF>
          <OneAppuisDAF>
               <Pt>10400 10000 10000</Pt>
               <NamePt>2</NamePt>
               <Incertitude>3 3
2</Incertitude>
          </OneAppuisDAF>
          <OneAppuisDAF>
               <Pt>10400 10400 10000</Pt>
               <NamePt>3</NamePt>
               <Incertitude>3 3
2</Incertitude>
          </OneAppuisDAF>
          <OneAppuisDAF>
               <Pt>10000 10400 10000</Pt>
               <NamePt>4</NamePt>
               <Incertitude>3 3
2</Incertitude>
          </OneAppuisDAF>
     </DicoAppuisFlottant>
</Global>
```

-

- **Surface Analysis: Measure Appuis –**

```
<?xml version="1.0" ?>
<SetOfMesureAppuisFlottants>

     <MesureAppuiFlottant1Im>
          <NameIm>1.JPG</NameIm>
         <OneMesureAF1I>
                <NamePt>1</NamePt>
                <PtIm>1349 3619</PtIm>
           </OneMesureAF1I>
        <OneMesureAF1I>
                <NamePt>2</NamePt>
                <PtIm>1346 226</PtIm>
           </OneMesureAF1I>
           <OneMesureAF1I>
                <NamePt>3</NamePt>
                <PtIm>4760 228</PtIm>
           </OneMesureAF1I>
           <OneMesureAF1I>
                <NamePt>4</NamePt>
                <PtIm>4733 3643</PtIm>
           </OneMesureAF1I>
     </MesureAppuiFlottant1Im>

     <MesureAppuiFlottant1Im>
          <NameIm>2.JPG</NameIm>
      <OneMesureAF1I>
                <NamePt>1</NamePt>
                <PtIm>4678 3477</PtIm>
           </OneMesureAF1I>
        <OneMesureAF1I>
                <NamePt>2</NamePt>
                <PtIm>1069 3502</PtIm>
           </OneMesureAF1I>
           <OneMesureAF1I>
                <NamePt>3</NamePt>
                <PtIm>1220 200</PtIm>
           </OneMesureAF1I>
      <OneMesureAF1I>
                <NamePt>4</NamePt>
                <PtIm>4496 182</PtIm>
            </OneMesureAF1I>
     </MesureAppuiFlottant1Im>

     <MesureAppuiFlottant1Im>
         <NameIm>3.JPG</NameIm>
         <OneMesureAF1I>
             <NamePt>1</NamePt>
             <PtIm>4636 269</PtIm>
         </OneMesureAF1I>
         <OneMesureAF1I>
             <NamePt>2</NamePt>
             <PtIm>4978 3433</PtIm>
         </OneMesureAF1I>
         <OneMesureAF1I>
             <NamePt>3</NamePt>
             <PtIm>1322 3548</PtIm>
         </OneMesureAF1I>
         <OneMesureAF1I>
             <NamePt>4</NamePt>
             <PtIm>1432 348</PtIm>
         </OneMesureAF1I>
     </MesureAppuiFlottant1Im>

     <MesureAppuiFlottant1Im>
         <NameIm>4.JPG</NameIm>
         <OneMesureAF1I>
             <NamePt>1</NamePt>
             <PtIm>1672 365</PtIm>
         </OneMesureAF1I>
         <OneMesureAF1I>
             <NamePt>2</NamePt>
             <PtIm>4848 424</PtIm>
         </OneMesureAF1I>
         <OneMesureAF1I>
             <NamePt>3</NamePt>
             <PtIm>4949 3623</PtIm>
         </OneMesureAF1I>
         <OneMesureAF1I>
             <NamePt>4</NamePt>
             <PtIm>1371 3513</PtIm>
         </OneMesureAF1I>
     </MesureAppuiFlottant1Im>


</SetOfMesureAppuisFlottants>
```

Appendix C

Workflow for Photogrammetric analysis of surface, part 2

In this appendix are the workflows and xml files for the full photogrammetric analysis in Matlab:

```
C1)   Main Workflow in matlab: Code 6

C2)   [DEM_orig] = DigitalElevationModel(image_orig,x_orig,y_orig,z_orig)

C3)   point_trans    = fmy_ply_read_xyzRGB(file_trans,1)

C4)   [NT,PosX1,PosY1]=Firstpos(image_trans, soft,p)

C5)   [temp,x_pm,y_pm]      = tempdisp(PosX1,PosY1 ,soft, i,j,image_trans)

C6)     [explo]   = explorationarea(image_orig, soft, x_pm,y_pm,delta)

C7)   [x_deform, y_deform] = Deforma(temp,explo,soft,delta)
```

CODE 6

```
clear all

%%%
```

```
file_trans     = ['T',num2str(t),'/MEC-Malt/NuageImProf_STD-MALT_Etape_9.ply'];
point_trans    = fmy_ply_read_xyzRGB(file_trans,1);
topo_trans     = point_trans.xyz ;

 x_trans       = topo_trans(1,:)';
 y_trans       = topo_trans(2,:)';
 z_trans       = topo_trans(3,:)';

%%%%%%%%%%%%%%%%%%%%%%%%%%%%%%%%%%%%%%%%%%%%%%%%%%%%%%%%%%%%%%%%%%%%%%%%%%%%
%
% Load orthophotos
%
%%%%%%%%%%%%%%%%%%%%%%%%%%%%%%%%%%%%%%%%%%%%%%%%%%%%%%%%%%%%%%%%%%%%%%%%%%%%

file_im_trans  = ['T',num2str(t),'/Ortho-MEC-Malt/Ortho-Eg-Test-Redr.tif'];
image_trans    = imread(file_im_trans);

[DEM_trans,x_mm,y_mm, x_p,y_p]      =
DigitalElevationModel(image_trans,x_trans,y_trans,z_trans);

%%%%%%%%%%%%%%%%%%%%%%%%%%%%%%%%%%%%%%%%%%%%%%%%%%%%%%%%%%%%%%%%%%%%%%%%%%%%
%
%Template is defined within the image with deformation (Image_trans)
%
%%%%%%%%%%%%%%%%%%%%%%%%%%%%%%%%%%%%%%%%%%%%%%%%%%%%%%%%%%%%%%%%%%%%%%%%%%%%

[NT,PosX1,PosY1]=Firstpos(image_trans, soft,p);
xDisp          = zeros(NT(1), NT(2));
yDisp          = zeros(NT(1), NT(2));
zDisp          = zeros(NT(1), NT(2));
x              = zeros(NT(1), NT(2));
y              = zeros(NT(1), NT(2));
z              = zeros(NT(1), NT(2));

%%%%%%%%%%%%%%%%%%%%%%%%%%%%%%%%%%%%%%%%%%%%%%%%%%%%%%%%%%%%%%%%%%%%%%%%%%%%
%
% For-loop calculating displacements of the templates
%
%%%%%%%%%%%%%%%%%%%%%%%%%%%%%%%%%%%%%%%%%%%%%%%%%%%%%%%%%%%%%%%%%%%%%%%%%%%%


for i = 7:NT(1)-6
   for j = 7:NT(2)-6


%%%%%%%%%%%%%%%%%%%%%%%%%%%%%%%%%%%%%%%%%%%%%%%%%%%%%%%%%%%%%%%%%%%%%%%%%%%%
%
% Displaying the template
%
```

```
%%%
```

```
    %%%%
```

DEM

```
function [DEM,x_mm,y_mm,x_p,y_p] = DigitalElevationModel(image_ortho,x,y,z);

%%%
```

```
%%%%%%%

x_loc_mm = (x_min:pdeltax:x_max);
y_loc_mm = (y_min:pdeltay:y_max);

x_mm = ones(length(y_loc_mm),1)* x_loc_mm ;
y_mm = y_loc_mm'*ones(1,length(x_loc_mm)) ;

F = TriScatteredInterp(x,y,z);


DEM = F(x_mm,y_mm);

end
```

FIGURE C.1: Matlab

PLY

```
function S= fmy_ply_read_xyzRGB(nameply,fic_binary)
% Amelie Neuville, 06 August 2013
% Purpose: read ply file generated by MicMac, with 3 float and 3 or 4 uchar
% on each line
% It is possible as well to use this file if your ply file is in
% txt format, but this option was just written quickly
% so check if it is OK as well for you - check number of headlines
% Can be used more generally to read binary file with n float and n' uchar
% per line. Do do so, test on header lines needs to be changed
%
% Input
%%%%%%%%
% nameply: path+name of the ply file
% fic_binary: can be 1 or other value.
% put fic_binary = 1 if it is a binary file with little endian format with some
% headlines written in txt
% else: text file
%
% CAUTION see the header line format of the files below and check your
% file format before using this function.
% Note that reading a binary
% file is faster than reading a text file !
%
%
% Exemple of Header line expected for binary file:
% Note that It is really important that the header file contains
% the fields
% 'element vertex'
% 'property float' (or/and) 'property uchar'
%  the rest does not really matter
%%%%%%%%%%%%%%%%%%%%%%%%%%%%%%%%%%%%%%%%%%%%%%%%%%%%%%%%%%%%%%%%%%%%%%%%%%%%%%%
   % ply
   % format binary_little_endian 1.0
   % comment VCGLIB generated
   % element vertex 4604459
   % property float x
   % property float y
   % property float z
   % property uchar red
   % property uchar green
   % property uchar blue
   % element face 0
   % property list uchar int vertex_indices
   % end_header
   %
```

```
% if you want to read text file, see the last part of the code,
% corresponding to else
%
% Output
%%%%%%%%%
% This function returns a structure with the following fields:
% S.xyz (float vector that contains x, y, z position)
% S.RGB (uint8 vector that contains RGB colors and alpha, if there is an alpha channel)
% if you want RGB as double later, simply use double(S.RGB)
%
% Example:
%%%%%%%%%%
% S=fmy_ply_read_xyzRGB('toto.ply',1); % toto.ply in binary format
% S=fmy_ply_read_xyzRGB('toto.ply',0); % toto.ply in text format
% Color=S.RGB;
% x=S.xyz(1,:);
% y=S.xyz(2,:);
% z=S.xyz(3,:);
% n=length(x);
disp(nameply);

if fic_binary==1
   fid=fopen(nameply,'r','ieee-le.l64'); % open binary file with little endian format
   ferror(fid)
   % File has a mixt format, with text and binary data
   %
   % Apparently, fopen and fgets handle the header text lines, even
   % if open as binary file (portable ????? Not sure at all !)  If it
   %does not work, just open the file first as text file, read
   %headerlines, close and reopen the file as binary file
   tline='';
   length_header=0;
   floatnb=0;
   ucharnb=0;
   while (~feof(fid) && (strncmp(tline,'end_header',10)~=1))
      if(feof(fid))
         error('In fmy_ply_readRGB, home-made error. End of file reached before nb of vortex could be
read, check the header file')
      end
      % Note: depending on the headlines you want to read, consider also
      % using (~ismember('#',tline )), (max(isstrprop(tline,
      % 'alpha'))~=1)),...
      length_header=length_header+1;
      tline = fgetl(fid);
      disp(tline)
      if (length(tline)>15 &&  strncmp(tline,'element vertex',14)==1)
         n=str2num(tline(16:end));
      end
      % check the number of float fields (=floatnb) (check done from the header
```

```
        % lines)
         if (length(tline)>15 &&  strncmp(tline,'property float',14)==1)
            if ucharnb==0
              floatnb=floatnb+1;
            else
               error('In fmy_ply_readRGB, home-made error, format should be 3 floats and 3 or 4 uchar on
the same line')
            end
         end
         % check that the uchar fields comes after 3 floats, and check the
         % number of uchar field (=ucharnb)
         if (length(tline)>15 &&  strncmp(tline,'property uchar',14)==1)
            if floatnb==3
              ucharnb=ucharnb+1;
            else
               error('In fmy_ply_readRGB, home-made error, format should be first 3 floats and 3 or 4
uchar on the same line')
            end
         end
        % 3 float and 3 or 4 uchar are expected
    end
    str=sprintf('\nOn each line, %d floats and %d uchar will be read\n%d lines\n',floatnb,ucharnb,n);
    disp(str);
    %tic
    % Declaration of matrix
     S.RGB=repmat(uint8(0),ucharnb,n); %uint8 format for RGB field
     S.xyz=ones(floatnb,n);

     % Slow loop, replaced by matrix reading
%     for i = 1:n
%         S.xyz(i,1:3)=fread(fid, 3, 'float32');
%         S.RGB(i,1:4)=fread(fid, 4, 'uchar');
%     end
    pos1=ftell(fid); % position in the file after the header lines

    % read xyz
    str=sprintf('%d*float32', floatnb);
    S.xyz=fread(fid,[floatnb,n],str,ucharnb);% for n times: read 3 float 32 and skip ucharnb uchar (unit
in bytes)
                                    % ex: ucharnb=4, 4*uchar = 4*8 bits = 4*1 bytes
    fseek(fid, pos1+floatnb*4,'bof'); % comes back to the beginning, after header + skip floatnb floats
(unit in bytes)
                                % ex floatnb=3, skip 3*4=12 bytes

    % read RGB and alpha, if there is an alpha channel
    str=sprintf('%d*uchar', ucharnb);
    S.RGB=uint8(fread(fid,[ucharnb,n],str,floatnb*4))% for n times: read ucharnb (ex: ucharnb=4) uchar
and skip  floatnb floats (unit in bytes)
                                        % ex. floatnb=3, ucharnb=4, 3 float = 3*4 bytes
```

```
   pos2=ftell(fid); % pos2-pos1 (value in bytes) should be equal to
   % number of lines n * (floatnb float + ucharnb* uchar)=n*16 bytes if ucharnb=4 and floatnb=3;


   % Rough check if there is basic errors in the reading
   % Well, this test will detect some errors, but I still assume that the
   % user has checked the file format before using this function !
   if ((pos2-pos1)~=n*(floatnb*4+ucharnb) || length(S.xyz) < n || length(S.RGB) <n)
      if(pos2-pos1)~=n*(floatnb*4+ucharnb)
         str=sprintf('pos2-pos1=%d, n=%d, nb of uchar=%d, nb of float=%d, n*(floatnb*4+ucharnb)=
%d',pos2-pos1, n, ucharnb, floatnb, n*(floatnb*4+ucharnb));
         disp(str);
      end
      if (length(S.xyz)<n)
         str=sprintf('length(S.xyz)=%d, n=%d',length(S.xyz),n);
         disp(str);
      end
      if (length(S.RGB)<n)
         str=sprintf('length(S.xyz)=%d, n=%d',length(S.RGB),n);
         disp(str);
      end
      str=sprintf('In fmy_ply_readRGB, home-made error, problem with the ply file:\nthe number of
data read is not right\nWrong file format ?')
      error(str);
   end
   %toc
   fclose(fid);
else % Text format % This part is not written in an flexible way,
   % it is just designed to read a txt file with 14 header lines
   % and 6 columns: 3 as double, 3 as uint8
   % Header lines & format digits:
   %%%%%%%%%%%%%%%%%%%%%%%%%%%%%%%%
   % ply
   % format ascii 1.0
   % comment VCGLIB generated
   % element vertex 4604459
   % property float x
   % property float y
   % property float z
   % property uchar red
   % property uchar green
   % property uchar blue
   % property uchar alpha
   % element face 0
   % property list uchar int vertex_indices
   % end_header
   % 10025.7 9972.75 10032.5 114 47 8 255
   % 10025.5 9972.82 10031.7 116 49 8 255
```

```
   M = dlmread(nameply,'',14,0); % Check if you have indeed 14 header lines before using this !
   S.RGB=uint8(M(:,4:6))'; % Well, if you want to read alpha also, just change to
S.RGB=uint8(M(:,4:7));
                    % if you don't like uin8 format, or read something else than uint8, just remove
                    % uint8 cast
   S.xyz=M(:,1:3)';
end
```

FIRSTPOS

```
function [NT,Xtemp,Ytemp] = Firstpos(image_trans, soft, p)
%Calculate the number of templates in one image w/ overlap

% Input:
% soft = size of template
% image_trans is the translated image with displacement
% p = overlap in desimals

%Output:
% NT = number of templates
% Xtemp = matrix of most left pixel in each template in x direction
% Ytemp = matrix of upper most pixel in each template in y direction

%image=imread(Image); % Only needed if the image is not loaded in code or
                      %in other function

%%%%%%%%%%%%%%%%%%%%%%%%%%%%%%%%%%%%%%%%%%%%%%%%%%%%%%%%%%%%%%%%%%%%%%%%
%%%%%% Y direction


ny = size(image_trans,1);   % calculates the number of pixels along y direction


NTy = 1;                    % Calculates the down position of first template
posy(NTy)= soft;


while max(posy)<=ny         % Loop that calculates the down position of the other templates with a
                            % condition that states that the max value of the down position of y is the size of the
   NTy = NTy + 1;           % image in pixels, ny
   posy(NTy) = soft + (NTy-1)*soft*(1-p);

end


Ytemp = posy(1:end-1)-soft+1; %Calculate a matrix of the most upper positions of the template


NT(1)   = NTy-1;            % Calculates the number of templates in the image along vertical


%%%%%%%%%%%%%%%%%%%%%%%%%%%%%%%%%%%%%%%%%%%%%%%%%%%%%%%%%%%%%%%%%%%%%%%%
%%%%%%%%%%%% X direction
```

```
nx = size(image_trans,2);   % calculates the number of pixels along x direction in the image

NTx  = 1;                % Calculates the down position of first template.
posx(NTx)  = soft;         %Position of lower pixel of first template = size of template


while max(posx)<=nx         % Calculates the down position of the other templates
   NTx     = NTx + 1;
   posx(NTx)     = soft + (NTx-1)*soft*(1-p);
end

NT(2)   = NTx-1 ;          % Calculates the number of templates in the image along vertical


Xtemp = posx(1:end-1)-soft+1;      %Calculate the most left position of the templates

%%%
```

TEMPDISP

```
function [temp,x_pm,y_pm]= tempdisp(Xtemp, Ytemp,soft, i,j,image_trans)
% function that chooses and displays a template

%image = imread(image);
% Ytemp and Xtemp is created in the function Firstpos and gives a matrix of the
% uppermost and left points of each template: 2 matrixes

y_pm = Ytemp(i,j); %Finds the y position of the upper left pixel of the template
        % depending on the location i,j which defines the row and
        % column of the y matrix

x_pm = Xtemp(i,j); % Find the x position of the upper left pixel of the template
        % depending on the location i,j which defines the row and
        % column of the x matrix

temp = image_trans(y_pm:y_pm+soft-1,x_pm:x_pm+soft-1,:);

% : means take all into consideration
% image_orig is the original image without displacement
% y+soft-1 gives the down position of the template
% x+soft-1 gives the most right position of the template
% x and y gives the most upper left position of the template

% figure(1);
% imshow(temp); % displays the template


end
```

EXPLORATIONAREA

```
%Function that defines the exploration window and displays it

function [explo] = explorationarea (image_orig, soft, x,y,delta)

explo = image_orig(y-delta:y+soft-1+delta,x-delta:x+soft-1+delta,:);
% image_orig is the original image without displacement
% delta is the difference between the exp-area and the template
% x is the position of the most left pixel of the template, see function tempdisp
% y is the position of the upper most pixel of the template, see funct. tempdisp
% soft is the size of the template in pixels
% y-delta is the location of the most upper part of the exp area
% x-delta is the most left part of the exp area
% When defining a picture, remember that it consist of 3 elements: y, x and
% RGB

% figure(2);
% imshow(explo); % displays the exploration window derived from the original image

end
```

DEFORMA

```
function [deform_x, deform_y] = Deforma(temp,exp,soft,delta)

correl = normxcorr2(temp(:,:,2), exp(:,:,2)); % Finds the correlation matrix with RGB = 2, where the
contrast is largest

size_correl = size(correl);

% figure(4);
% surf(correl); % display 3d image of correlation matrix

% [max_c, imax] = max(abs(correl(:))); % Calculate the point and value of maximum correlation of the
matrix. Returns two points (numbers)
% [ypeak, xpeak] = ind2sub(size(correl),imax); % Convert the point value of the location into x and y
position in the matrix of the correlation
%
% deform_x = -(xpeak - (soft + delta)); % Finds the deformation in x direction by substracting the max
correl x position with the site of zero deformation soft + delta
% deform_y = ypeak - (soft + delta); % Finds the deformation in y direction by substracting the max
correl y position with the site of zero deformation soft + delta

x_ind = ones(size_correl(1),1)*(1:1:size_correl(2)); % matrix of the location of the deformation in the
x direction. Ones(row: the size
                                    % of correlation matrix i y direction, column = 1)
                                    %  *(1 to(by the step of 1) the size of the correlation matrix in the x
direction.
y_ind = (1:1:size_correl(1))'*ones(1,size_correl(2)); % matrix of the location of the deformation in the
y direction. 1 to (by the step of 1)
                                     %the size of the correlation matrix in the y-direction * ones(row: 1,
column = the size of the correlation matrix in x-direction)

x_indint = ones(10*size_correl(1)-9,1)*(1:0.1:size_correl(2)); % X-index-interpolated = Create more
point in between pixels to find sub-pixel resolution and a better max point.
y_indint = (1:0.1:size_correl(1))'*(ones(1,10*size_correl(2)-9));% Y-index-interpolated = create more
points in between pixels to find sub-pixel resolution and better max point.

inter_correl = interp2(x_ind,y_ind,correl,x_indint,y_indint,'spline'); % Interpolating the correlation
matrix to increase the density of points and thereby the resolution.
                                                    % Using 5 inputs: the two matrixes of x and y with the
location of the deformation, the correlation
                                                    % matrix and the two matrices with the new locations of
deformation
                                                     % spline tells the function to use the spline interpolation:


size_intercorr = size(inter_correl);          % Gives the size of the interpolated correlation matrix
```

Appendix D

Workflow for Photogrammetric analysis of Intrusion

Workflow for intrusion analysis in MicMac

```
export PATH=/Applications/MicMac/bin:$PATH

Tapioca All .*.JPG -1

Tapas Fraser .*.JPG Out=Ground

GCPBascule .*.JPG Ground Terrain-Ground Dico-Appuis.xml Mesure-
Appuis.xml

AperiCloud .*.JPG Terrain-Ground Out=AperiCloud.ply

MICMAC Micmac-POV.xml
```

Dico-Appuis for intrusion analysis in MicMac

```
      <?xml version="1.0" ?>
<Global>
     <DicoAppuisFlottant>
          <OneAppuisDAF>
               <Pt>10000 10000 9950</Pt>
               <NamePt>1</NamePt>
               <Incertitude>3 3 2</Incertitude>
          </OneAppuisDAF>
          <OneAppuisDAF>
               <Pt>10400 10000 9950</Pt>
               <NamePt>2</NamePt>
               <Incertitude>3 3 2</Incertitude>
          </OneAppuisDAF>
          <OneAppuisDAF>
               <Pt>10400 10400 9950</Pt>
               <NamePt>3</NamePt>
               <Incertitude>3 3 2</Incertitude>
          </OneAppuisDAF>
          <OneAppuisDAF>
               <Pt>10000 10400 9950</Pt>
               <NamePt>4</NamePt>
               <Incertitude>3 3 2</Incertitude>
          </OneAppuisDAF>
         <OneAppuisDAF>
             <Pt>10400 10000 9865</Pt>
             <NamePt>5</NamePt>
             <Incertitude>3 3 2</Incertitude>
         </OneAppuisDAF>
         <OneAppuisDAF>
             <Pt>10400 10400 9865</Pt>
             <NamePt>6</NamePt>
             <Incertitude>3 3 2</Incertitude>
         </OneAppuisDAF>
           <OneAppuisDAF>
             <Pt>10000 10400 9865</Pt>
             <NamePt>7</NamePt>
             <Incertitude>3 3 2</Incertitude>
         </OneAppuisDAF>
         <OneAppuisDAF>
             <Pt>10000 10000 9865</Pt>
             <NamePt>8</NamePt>
             <Incertitude>3 3 2</Incertitude>
         </OneAppuisDAF>

     </DicoAppuisFlottant>
</Global>
```

Mesure-Appuis for intrusion analysis

```
<?xml version="1.0" ?>
<SetOfMesureAppuisFlottants>

     <MesureAppuiFlottant1Im>

<NameIm>DSC_0001.JPG</NameIm>
        <OneMesureAF1I>
              <NamePt>5</NamePt>
              <PtIm>4553 3519</PtIm>
          </OneMesureAF1I>
        <OneMesureAF1I>
              <NamePt>6</NamePt>
              <PtIm>4590 467</PtIm>
          </OneMesureAF1I>
          <OneMesureAF1I>
              <NamePt>7</NamePt>
              <PtIm>1532 442</PtIm>
          </OneMesureAF1I>
          <OneMesureAF1I>
              <NamePt>8</NamePt>
              <PtIm>1514 3496</PtIm>
          </OneMesureAF1I>
     </MesureAppuiFlottant1Im>

    <MesureAppuiFlottant1Im>
        <NameIm>DSC_0003.JPG</NameIm>
        <OneMesureAF1I>
            <NamePt>5</NamePt>
            <PtIm>4366 649</PtIm>
        </OneMesureAF1I>
        <OneMesureAF1I>
            <NamePt>6</NamePt>
            <PtIm>1462 622</PtIm>
        </OneMesureAF1I>
        <OneMesureAF1I>
            <NamePt>7</NamePt>
            <PtIm>1309 3529</PtIm>
        </OneMesureAF1I>
        <OneMesureAF1I>
            <NamePt>8</NamePt>
            <PtIm>4528 3533</PtIm>
        </OneMesureAF1I>
    </MesureAppuiFlottant1Im>
```

```
<MesureAppuiFlottant1Im>
          <NameIm>DSC_0005.JPG</NameIm>
      <OneMesureAF1I>
              <NamePt>5</NamePt>
              <PtIm>4559 935</PtIm>
          </OneMesureAF1I>
       <OneMesureAF1I>
              <NamePt>6</NamePt>
              <PtIm>1768 788</PtIm>
          </OneMesureAF1I>
          <OneMesureAF1I>
              <NamePt>7</NamePt>
              <PtIm>1388 3302</PtIm>
          </OneMesureAF1I>
      <OneMesureAF1I>
              <NamePt>8</NamePt>
              <PtIm>4747 3470</PtIm>
          </OneMesureAF1I>
     </MesureAppuiFlottant1Im>

</SetOfMesureAppuisFlottants>
```

MicMac-POV.xml for intrusion analysis in MicMac

```
<ParamMICMAC>

<DicoLoc>
   <Symb> NumC=0015 </Symb>
   <Symb> NumMin=0012 </Symb>
   <Symb> NumMax=0021 </Symb>
   <Symb> Im=.*.JPG </Symb>
   <Symb> ImP=DSC_ </Symb>
   <Symb> ImF=.JPG </Symb>
   <Symb> MEC=3D </Symb>
   <Symb> OriIn=Terrain-Ground </Symb>
</DicoLoc>

<Section_Terrain>
      <IntervAltimetrie>
             <!-- Mandatory but unused -->
             <ZIncCalc>   0.0  </ZIncCalc>
      </IntervAltimetrie>
      <IntervSpecialZInv >
             <MulZMin >  0.3</MulZMin>
             <MulZMax > 3 </MulZMax>
      </IntervSpecialZInv>
     <Planimetrie>
         <MasqueTerrain>
             <MT_Image> ${ImP}${NumC}_Masq.tif </MT_Image>
             <MT_Xml> ${ImP}${NumC}_Masq.xml </MT_Xml>
         </MasqueTerrain>
     </Planimetrie>

</Section_Terrain>

<Section_PriseDeVue >
     <GeomImages> eGeomImageOri </GeomImages>
     <Images >

          <Im1> ${ImP}${NumC}${ImF} </Im1>
          <ImPat> ${Im} </ImPat>
          <Filter>
              <Min>  ${ImP}${NumMin}${ImF}  </Min>
              <Max>  ${ImP}${NumMax}${ImF} </Max>
           </Filter>
     </Images>


     <NomsGeometrieImage>
         <FCND_Mode_GeomIm>
```

Bibliography

Abdelmalak, M., R., M., Galland, O., and Bureau, D. (2012). Fracture mode analysis and related surface deformation during dyke intrusion: Results from 2d experimental modelling. *Earth and Planetary Science Letters*, 359-360(0):93 – 105.

Amelung, F., Jónsson, S., Zebker, H., and Segall, P. (2000). Widespread uplift and 'trapdoor'faulting on galapagos volcanoes observed with radar interferometry. *Nature*, 407(6807):993–996.

Aoki, Y., Takeo, M., Ohminato, T., Nagaoka, Y., and Nishida, K. (2013). Magma pathway and its structural controls of asama volcano, japan. *Geological Society, London, Special Publications*, 380(1):67–84.

Battaglia, J. and Bachèlery, P. (2003). Dynamic dyke propagation deduced from tilt variations preceding the march 9, 1998, eruption of the piton de la fournaise volcano. *Journal of Volcanology and geothermal Research*, 120(3):289–310.

Bonaccorso, A. (1998). Evidence of a dyke-sheet intrusion at stromboli volcano inferred through continuous tilt. *Geophysical Research Letters*, 25(22):4225–4228.

Bourke, P. (2014). Ply-polygon file format.

Burchardt, S., Tanner, D., and Krumbholz, M. (2010). Mode of emplacement of the slaufrudalur pluton, southeast iceland inferred from three-dimensional gps mapping and model building. *Tectonophysics*, 480(1-4):232–240. cited By (since 1996)3.

Cayol, V. and Cornet, F. (1997). 3d mixed boundary elements for elastostatic deformation field analysis. *International Journal of Rock Mechanics and Mining Sciences*, 34(2):275 – 287.

Cayol, V. and Cornet, F. (1998). Three-dimensional modeling of the 1983 - 1984 eruption at piton de la fournaise volcano, reunion island. *Journal of Geophysical Research: Solid Earth*, 103(B8):18025–18037.

Cecchi, E., van Wyk de Vries, B., Lavest, J.-M., Harris, A., and Davies, M. (2003). ¡ i¿ n¡/i¿-view reconstruction: a new method for morphological modelling and deformation measurement in volcanology. *Journal of volcanology and geothermal research*, 123(1):181–201.

CWU (2014). The pacific northwest geodetic array.

Delcamp, A., van Wyk de Vries, B., and James, M. R. (2008). The influence of edifice slope and substrata on volcano spreading. *Journal of Volcanology and Geothermal Research*, 177(4):925–943.

DeWitt, B. A. and Wolf, P. R. (2000). Elements of photogrammetry (with applications in gis).

Dieterich, J. H. and Decker, R. W. (1975). Finite element modeling of surface deformation associated with volcanism. *Journal of Geophysical Research*, 80(29):4094–4102.

Donnadieu, F., Kelfoun, K., van Wyk de Vries, B., Cecchi, E., and Merle, O. (2003). Digital photogrammetry as a tool in analogue modelling: applications to volcano instability. *Journal of Volcanology and Geothermal Research*, 123(1 - 2):161 – 180. Volcanic hazards: Monitoring, prediction and mitigation.

Duyck, B. (2014). Insar image showing the deformation of the volcano longonot / east-african rift between 2004 e 2006, envisat autoc2.

Dzurisin, D. (2006). *Volcano deformation: new geodetic monitoring techniques*. Springer.

Dzurisin, D., Westphal, J. A., and Johnson, D. J. (1983). Eruption prediction aided by electronic tiltmeter data at mount st. helens. *Science*, 221(4618):1381–1383.

Ebmeier, S., Biggs, J., Mather, T., and Amelung, F. (2013). Applicability of insar to tropical volcanoes: insights from central america. *Geological Society, London, Special Publications*, 380(1):15–37.

Galland, O. (2012). Experimental modelling of ground deformation associated with shallow magma intrusions. *Earth and Planetary Science Letters*, 317:145–156.

Galland, O., Cobbold, P. R., de Bremond d'Ars, J., and Hallot, E. (2007). Rise and emplacement of magma during horizontal shortening of the brittle crust: Insights from experimental modeling. *Journal of Geophysical Research: Solid Earth (1978–2012)*, 112(B6).

Galland, O., Cobbold, P. R., Hallot, E., de Bremond d'Ars, J., and Delavaud, G. (2006). Use of vegetable oil and silica powder for scale modelling of magmatic intrusion in a deforming brittle crust. *Earth and Planetary Science Letters*, 243(3 å4):786 – 804.

Galland, O., De Bremond d'Ars, J., Cobbold, P. R., and Hallot, E. (2003). Physical models of magmatic intrusion during thrusting. *Terra Nova*, 15(6):405–409.

Galland, O., Planke, S., Neumann, E.-R., and Malthe-Sørenssen, A. (2009). Experimental modelling of shallow magma emplacement: application to saucer-shaped intrusions. *Earth and Planetary Science Letters*, 277(3):373–383.

Globesar (2014). Sbas-insar for surface displacement monitoring.

Graveleau, F. and Dominguez, S. (2008). Analogue modelling of the interaction between tectonics, erosion and sedimentation in foreland thrust belts. *Comptes Rendus Geoscience*, 340(5):324–333.

Gressier, J., M. R. B. L. Y. J. (2010). Control of pore fluid pressure on depth of emplacement of magmatic sills: An experimental approach. *Tectonophysics*, 489(1–4):1 – 13.

Harrison, J. C. (1976). Cavity and topographic effects in tilt and strain measurement. *Journal of Geophysical Research*, 81(2):319–328.

Hubbert, M. K. and Willis, D. G. (1972). Mechanics of hydraulic fracturing.

Jordan, R. and Kieffer, H. H. (1981). Topographic changes at mount st. helens: Large-scale photogrammetry and digital terrain models. *US Geol. Surv. Prof. Pap*, 1250:135–141.

Kavanagh, J. L., Menand, T., and Sparks, R. S. J. (2006). An experimental investigation of sill formation and propagation in layered elastic media. *Earth and Planetary Science Letters*, 245(3):799–813.

Krantz, R. W. (1991). Measurements of friction coefficients and cohesion for faulting and fault reactivation in laboratory models using sand and sand mixtures. *Tectonophysics*, 188(1):203–207.

Lague, D., Crave, A., and Davy, P. (2003). Laboratory experiments simulating the geomorphic response to tectonic uplift. *Journal of Geophysical Research: Solid Earth (1978–2012)*, 108(B1):ETG–3.

Larson, K. M., Poland, M., and Miklius, A. (2010). Volcano monitoring using gps: Developing data analysis strategies based on the june 2007 kīlauea volcano intrusion and eruption. *Journal of Geophysical Research: Solid Earth (1978–2012)*, 115(B7).

Lu, Z., Dzurisin, D., Biggs, J., Wicks, C., and McNutt, S. (2010). Ground surface deformation patterns, magma supply, and magma storage at Okmok volcano, Alaska, from InSAR analysis: 1. Intereruption deformation, 1997-2008. *Journal of Geophysical Research*, 115.

Massonnet, D. and Feigl, K. L. (1998). Radar interferometry and its application to changes in the earth's surface. *Reviews of Geophysics*, 36(4):441–500.

Mathieu, L. and van Wyk de Vries, B. (2011). The impact of strike-slip, transtensional and transpressional fault zones on volcanoes. part 1: Scaled experiments. *Journal of Structural Geology*, 33(5):907–917.

Mathieu, L., van Wyk de Vries, B., Holohan, E. P., and Troll, V. R. (2008). Dykes, cups, saucers and sills: Analogue experiments on magma intrusion into brittle rocks. *Earth and Planetary Science Letters*, 271(1-4):1 – 13.

Merle, O. and Vendeville, B. (1995). Experimental modelling of thin-skinned shortening around magmatic intrusions. *Bulletin of Volcanology*, 57(1):33–43.

Mogi, K. (1958). Relations between the eruptions of various volcanoes and the deformations of the ground surfaces around them.

Moore, J. G. and Albee, W. C. (1981). Topographic and structural changes, march-july 1980—photogrammetric data. *US Geol. Surv. Prof. Pap*, 1250:123–134.

Okada, Y. (1985). Surface deformation due to shear and tensile faults in a half-space. *Bulletin of the seismological society of America*, 75(4):1135–1154.

Owen, S., Segall, P., Freymueller, J., Mikijus, A., Denlinger, R., Árnadóttir, T., Sako, M., and Bürgmann, R. (1995). Rapid deformation of the south flank of kilauea volcano, hawaii. *Science*, 267(5202):1328–1332.

Owen, S., Segall, P., Lisowski, M., Miklius, A., Murray, M., Bevis, M., and Foster, J. (2000). January 30, 1997 eruptive event on kilauea volcano, hawaii, as monitored by continuous gps. *Geophysical Research Letters*, 27(17):2757–2760.

Pedersen, R. and Sigmundsson, F. (2006). Temporal development of the 1999 intrusive episode in the eyjafjallajökull volcano, iceland, derived from insar images. *Bulletin of Volcanology*, 68(4):377–393.

Pesci, A., Fabris, M., Conforti, D., Loddo, F., Baldi, P., and Anzidei, M. (2007). Integration of ground-based laser scanner and aerial digital photogrammetry for topographic modelling of vesuvio volcano. *Journal of Volcanology and Geothermal Research*, 162(3–4):123 – 138.

Pyle, D. M., Mather, T. A., and Biggs, J. (2013). Remote sensing of volcanoes and volcanic processes: integrating observation and modelling–introduction. *Geological Society, London, Special Publications*, 380(1):1–13.

Reber, J. E., Galland, O., Cobbold, P. R., and Le Carlier de Veslud, C. (2013). Experimental study of sheath fold development around a weak inclusion in a mechanically layered matrix. *Tectonophysics*, 586:130–144.

Reuter, R. (2014). 3d modellen - stereoparen.

Rivalta, E., Böttinger, M., and Dahm, T. (2005). Buoyancy-driven fracture ascent: Experiments in layered gelatine. *Journal of volcanology and geothermal research*, 144(1):273–285.

Rossi, D. and Storti, F. (2003). New artificial granular materials for analogue laboratory experiments: aluminium and siliceous microspheres. *Journal of Structural Geology*, 25(11):1893–1899.

Schellart, W. (2000). Shear test results for cohesion and friction coefficients for different granular materials: scaling implications for their usage in analogue modelling. *Tectonophysics*, 324(1):1–16.

Schuckman, K.; Renslow, K. (2014). The pacific northwest geodetic array.

Segall, P. (2013). Volcano deformation and eruption forecasting. *Geological Society, London, Special Publications*, 380(1):85–106.

Segall, P., Cervelli, P., Owen, S., Lisowski, M., and Miklius, A. (2001). Constraints on dike propagation from continuous gps measurements. *Journal of Geophysical Research: Solid Earth (1978–2012)*, 106(B9):19301–19317.

Segall, P. and Davis, J. L. (1997). Gps applications for geodynamics and earthquake studies. *Annual Review of Earth and Planetary Sciences*, 25(1):301–336.

sensing core curriculum, R. (2014). Volume 1 module 7 stereoscopy and height measurement.

Sigmundsson, F., Einarsson, P., and Bilham, R. (1992). Magma chamber deflation recorded by the global positioning system: The hekla 1991 eruption. *Geophysical research letters*, 19(14):1483–1486.

Sigmundsson, F., Hreinsdóttir, S., Hooper, A., Árnadóttir, T., Pedersen, R., Roberts, M. J., Óskarsson, N., Auriac, A., Decriem, J., Einarsson, P., et al. (2010). Intrusion triggering of the 2010 eyjafjallajokull explosive eruption. *Nature*, 468(7322):426–430.

space agency, E. (2014). Ers-1 sar interferometry orbit listing user note.

Sturkell, E., Einarsson, P., Sigmundsson, F., Geirsson, H., Ólafsson, H., Pedersen, R., de Zeeuw-van Dalfsen, E., Linde, A. T., Sacks, S. I., and Stefánsson, R. (2006). Volcano geodesy and magma dynamics in iceland. *Journal of Volcanology and Geothermal Research*, 150(1–3):14 – 34. The Changing Shapes of Active Volcanoes Recent Results and Advances in Volcano Geodesy.

Takada, A. (1990). Experimental study on propagation of liquid-filled crack in gelatin: Shape and velocity in hydrostatic stress condition. *Journal of Geophysical Research: Solid Earth (1978–2012)*, 95(B6):8471–8481.

Takada, A. (1994). Development of a subvolcanic structure by the interaction of liquid-filled cracks. *Journal of volcanology and geothermal research*, 61(3):207–224.

Tele-Rilevamento-Europa (2014). Insar evolution.

Tortini, R., Bonali, F., Corazzato, C., Carn, S., and Tibaldi, A. (2013). An innovative application of the kinect in earth sciences: quantifying deformation in analogue modelling of volcanoes. *TERRA nova*.

Wauthier, C., Cayol, V., Poland, M., Kervyn, F., d'Oreye, N., Hooper, A., Samsonov, S., Tiampo, K., and Smets, B. (2013). Nyamulagira's magma plumbing system inferred from 15 years of insar. *Geological Society, London, Special Publications*, 380(1):39–65.